Heavy rare earth elements and the sources of continental flood basalts

Heinonen, Jussi S.

2022-10-01

OXFORD

Heavy Rare Earth Elements and the Sources of Continental Flood Basalts

Jussi S. Heinonen[1,2,*], Eric L. Brown[3], Sanni T. Turunen[1] and Arto V. Luttinen[1]

[1]Finnish Museum of Natural History, University of Helsinki, PO Box 44, 00014 Helsinki, Finland
[2]Department of Geosciences and Geography, University of Helsinki, PO Box 64, 00014 Helsinki, Finland
[3]Department of Geosciences, Aarhus University, Høegh-Guldbergs Gade 2, DK-8000 Aarhus C, Denmark

*Corresponding author. E-mail: jussi.s.heinonen@helsinki.fi

Abstract

Heavy rare earth elements (HREEs) in mafic and ultramafic volcanic rocks are useful recorders of mantle source processes because their ratios are not easily modified by differentiation. Here we utilize REEBOX PRO, a simulator of adiabatic decompression melting of the mantle, to study the behavior of HREEs in the formation of continental flood basalt (CFB) parental magmas in the mantle. We simulate partial melting of depleted peridotite, pyrolitic peridotite, pyroxenite, and peridotite-pyroxenite mixtures at mantle potential temperatures of 1350–1650°C and lithospheric thicknesses of 50–150 km, and compare the results to natural data. Many large igneous provinces are typified by low-Ti and high-Ti CFBs with contrasting HREE patterns. Our results show that low-Ti CFBs originate mainly from peridotitic sources. Flat mid-ocean ridge basalt-like HREE patterns typical of low-Ti CFBs can be generated beneath thick lithosphere (∼100 km), given that mantle potential temperatures are high (>1500°C) and garnet is completely consumed from the source. We thus challenge the common interpretation that flat HREE patterns always indicate shallow sources for CFB parental magmas. High-Ti CFBs require pyroxenite-bearing sources (≥10%). Contrary to a common view, their steep oceanic island basalt-like HREE patterns can be generated beneath quite a thin lithosphere (∼50 km), which is due to increased garnet stability in pyroxenite sources. When applied to CFBs of the Karoo large igneous province, the results are compatible with a model where a mantle plume penetrates a progressively thinning Gondwana lithosphere.

Keywords: rare earth elements, modeling, low Ti, high Ti, continental flood basalts

INTRODUCTION

Rare earth elements (REEs) are composed of Y, Sc, and the lanthanides La − Lu (Pm not found in nature). REEs are probably the single most important group of trace elements used for geochemical and petrogenetic research of igneous rocks. This stems from these elements having very uniform chemical and physical properties, yet their mineral-melt partitioning deviates enough to reveal histories of partial melting and crystallization. The compatibility of REEs in rock-forming silicate minerals generally increases relative to the atomic number so that light REEs (LREEs: La − Sm) are usually more incompatible than the heavy REEs (HREEs: Eu − Lu; Y and Sc are also rather compatible and considered as HREEs despite them being lighter) (see, e.g. Rollinson & Pease, 2021). This is exemplified by, for example, higher LREE/HREE in a mantle partial melt compared to its residue. This behavior is most pronounced in the presence of residual garnet that exhibits mineral-liquid partition coefficients (K_D) greater than 1 for HREEs in general, for example, as high as 1000 for Lu in certain basaltic liquids (Klimm et al., 2008).

Because of the strong control of garnet on HREE fractionation, REEs have become essential elements in determining whether or not mantle melts have formed in the presence of garnet. The transition from garnet peridotite (lherzolite) to spinel peridotite with decreasing pressure at near-solidus temperatures has been constrained to begin at around 3.1–2.6 GPa, which corresponds

to depths of about 100–80 km (Robinson & Wood, 1998; Klemme & O'Neill, 2000). The primary melts of mid-ocean ridge basalts (MORBs) derive dominantly from rather shallow spinel or plagioclase lherzolite sources (e.g. Fujii, 1989; Krein et al., 2020). The primary melts of oceanic island basalts (OIBs) are generated beneath thicker oceanic lithosphere and often under higher mantle potential temperatures. Thus, OIBs derive dominantly from garnet-bearing lithologies: garnet lherzolite or garnet pyroxenite (or eclogite) or their mixture (e.g. Herzberg, 2006; Dasgupta et al., 2010; Mallik & Dasgupta, 2012). This fundamental petrogenetic difference is reflected in the REE patterns of MORBs and OIBs: MORBs exhibit flat HREE patterns, whereas OIBs exhibit steep HREE patterns that plunge toward relatively low Lu (Fig. 1a, b).

Continental flood basalt (CFB) provinces are among the largest manifestations of mantle-derived volcanism. Their eruptive volumes are enormous (>10^6 km³); they form within rather short periods of geological time (duration of the main magmatic pulse around 1–5 Ma); their emissions contribute to mass extinctions; and they have frequently been precursors of continental break-up (Bryan & Ernst, 2008; Bryan et al., 2010). CFBs exhibit very heterogeneous trace element and isotopic compositions that reflect their derivation from heterogeneous sources in the sublithospheric and variably metasomatized lithospheric mantle and subsequent contamination by crustal materials, which readily modifies the LREE concentrations of
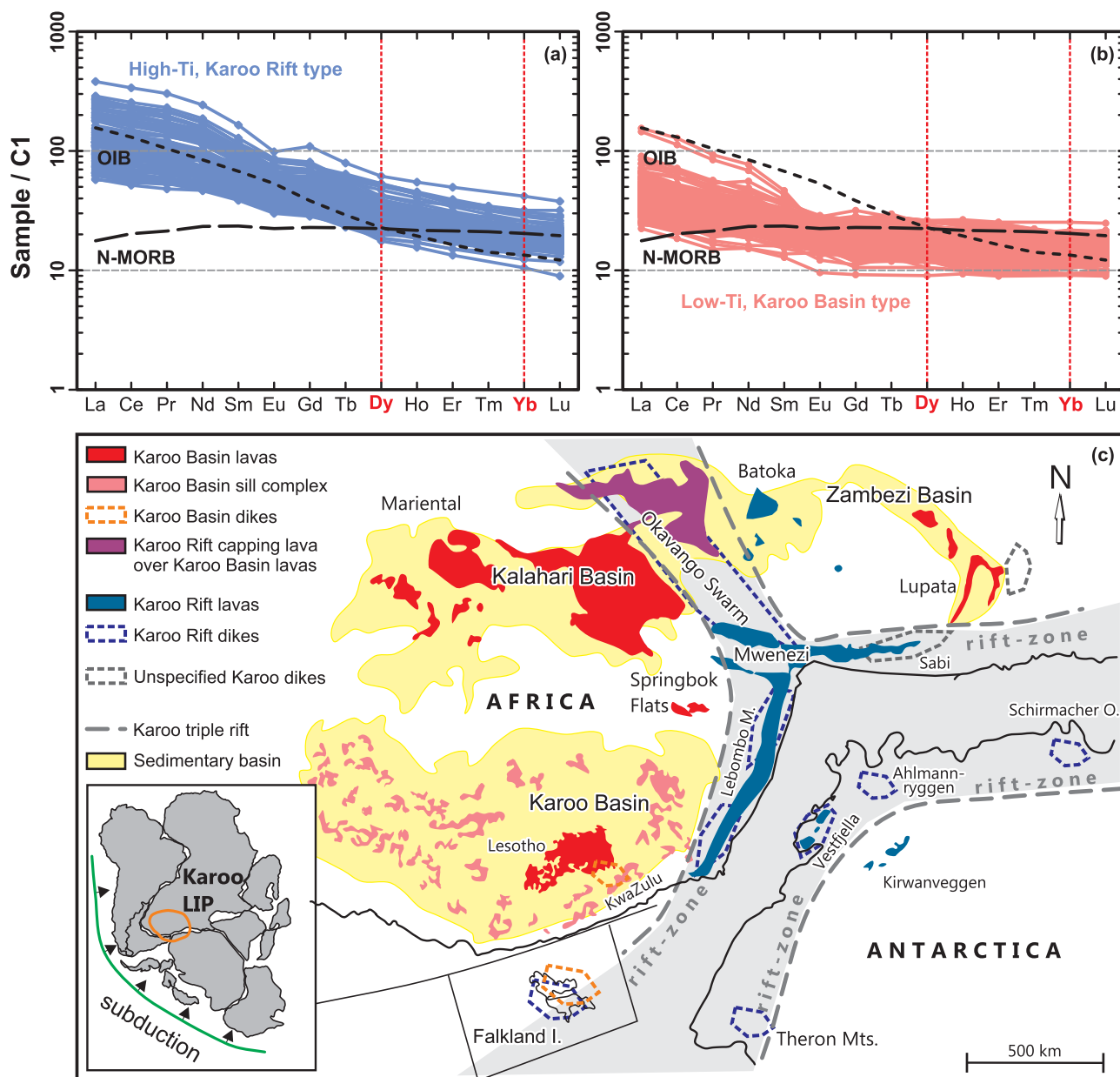
Figure 1. REE (Y and Sc not included) patterns of selected (a) high-Ti CFBs and related dikes of the Rift subprovince and (b) low-Ti CFBs and related sills of the Basin subprovince of the Karoo LIP. Average OIB (Sun & McDonough, 1989) and mean N-MORB (Gale *et al.*, 2013) shown for comparison. Normalization values after C1 chondrite of McDonough & Sun (1995). Dy and Yb are highlighted as indicators of flat (($Dy/Yb)_N \approx 1$; e.g. N-MORB) vs. steep (($Dy/Yb)_N > 1$; e.g. OIB) HREE patterns. Karoo CFB data sources: Sweeney et al. (1994), Rehácek (1995), Luttinen et al. (1998, 2015), Riley et al. (2006), Jourdan et al. (2007a), Galerne et al. (2008), Neumann et al. (2011), and Luttinen (2018). For full data compilation, see Supplementary Data. (c) Distribution of Karoo Basin and Karoo Rift CFB lavas and related intrusive rocks in 180 Ma Gondwana reconstruction. The Karoo Rift CFBs are seaward-dipping lavas (e.g. Sabi, Lebombo, Vestfjella) and dike swarms associated with a triple rift structure (Burke & Dewey, 1973). The Karoo Basin CFBs are lavas, sills, and dikes in the main Karoo, Kalahari, and Zambezi Basins. The division is based on Luttinen (2018) and reconstruction on Lawver et al. (1998).

CFB magmas. Concentrations of HREEs in crustal materials are generally low (Rudnick & Gao, 2003), however, and thus the mantle-derived HREE signatures of CFB primary magmas are not easily overwritten by contamination. There is a first-order division into low-Ti and high-Ti CFBs, with the high-Ti types generally exhibiting steeper HREE curves (Fig. 1a) thereby reflecting a more important role for residual garnet in their generation. Accordingly, high-Ti types have been interpreted to represent melts derived by lower degree melting at greater depths (e.g. Melluso *et al.*, 2006; Jourdan *et al.*, 2007a; Shellnutt & Jahn, 2011; Marzoli *et al.*, 2019; Zhang *et al.*, 2019). Many low-Ti CFBs possess flat HREE patterns

similar to those of MORBs (Fig. 1b). This has generally been suggested to point to the generation of these magmas at relatively shallow depths, in the stability field of spinel peridotite, either in sub-continental lithospheric mantle (SCLM) or in asthenosphere beneath significantly thinned lithosphere (e.g. Tegner *et al.*, 1998; Melluso *et al.*, 2006; Jourdan *et al.*, 2007a; Neumann *et al.*, 2011; Shellnutt *et al.*, 2014).

Most existing trace element models of CFB magma genesis apply simplified batch or fractional melting equations without considering the thermodynamics of the modeled system or the polybaric nature of mantle melting. In the current study, we

overcome these limitations by modeling the effects of mantle temperature, pressure, and composition on HREE patterns of mantle-derived melts using REEBOX PRO, a forward melting model of thermally and lithologically variable upwelling mantle (Brown & Lesher, 2016). We focus our attention on conditions relevant to CFB magmatism, where the pre-existing lithosphere is thick and mantle potential temperatures are high. We challenge the idea that flat HREE patterns indicate shallow sources for CFB parental magmas and, instead, suggest that such magmas can also originate from beneath a thick lithosphere when garnet is completely consumed from a peridotitic source under high mantle potential temperatures. Application of the model to the Jurassic Karoo province shows that the range of Dy/Yb ratios of the high-Ti and low-Ti CFBs can be replicated under thick (100 km) lithosphere by varying temperature and mantle source composition. However, we argue that our overall results point toward a progressively, but not necessarily uniformly, thinning lithosphere during Karoo magmatism.

METHODS
REEBOX PRO—model background

REEBOX PRO is a forward model that simulates adiabatic decompression melting of homogeneous or heterogeneous mantle sources containing anhydrous peridotite (lherzolite), hydrous peridotite (lherzolite), pyroxenite (three types: G2, MIX1G, and KG1 pyroxenite), and/or residual harzburgite (Brown & Lesher, 2016; Brown et al., 2020). In addition to distinguishing between anhydrous and hydrous peridotite, the model also allows the user to specify melting of pyrolite peridotite, or Depleted MORB Mantle (DMM) peridotite, which have slightly different mineralogies and solidi. Additional key model inputs include mantle potential temperature and the trace element abundances and isotopic compositions of the source rocks. Assuming all specified lithologies are in thermal equilibrium, but not in chemical equilibrium, the program uses thermodynamic and experimental constraints to quantify their polybaric productivities (dF/dP) at discrete decompression steps (every 0.01 GPa) between the deepest solidus and base of the lithosphere. The mineral mode parameterizations on the solidus are based on experimental constraints and thermodynamic modeling with PERPLE_X (see Brown & Lesher, 2016). Using experimentally constrained mineral modes, melting modes, and either temperature-dependent or static mineral-melt partition coefficients the model then calculates the compositions of instantaneous melts generated by incremental batch melting of each lithology during each decompression step. For each lithology, instantaneous melts are mixed along the melting column to provide a 'column-accumulated' melt composition at the top of the melting column. Finally, for an assumed style of mantle flow (passive or active) and half-spreading rate (for active upwelling only), the bulk igneous crust thickness and composition is calculated by pooling together all column-accumulated melts derived from all lithologies (pooled melts).

Of particular relevance for the modeling presented here is the stability of garnet in the different source lithologies. For the pyrolite and DMM peridotite lithologies, garnet is stable at the solidus down to 2.3 GPa and 2.5 GPa, respectively. For the three pyroxenites included in REEBOX PRO, garnet remains stable at the solidus to lower pressures than either of these peridotites. For G2 and MIX1G pyroxenite, garnet is a solidus phase at all pressures, whereas for KG1 garnet is stable at the solidus at P > 2.19 GPa (Brown & Lesher, 2016; Brown et al., 2020). The reader is referred to Brown & Lesher (2016) for model benchmarks and further details.

REEBOX PRO—model input

For modeling of HREE behavior in mantle melting in CFB settings, we used the following input and model choices. These are given and discussed in the order they appear in the REEBOX PRO v.1.1 user interface and are illustrated in Fig. 2.

To provide a good overview on the melting of different mantle sources, we selected five different initial source models (Fig. 2a). We focused on sublithospheric sources since modeling of metasomatized lithospheric sources is difficult due to large uncertainties regarding the initial source composition. Three of the sources are pure end-members: depleted mantle lherzolite (trace element composition of depleted MORB mantle (DMM); Workman & Hart, 2005), pyrolite (trace element composition of primitive mantle (PM); McDonough & Sun, 1995), and G2 pyroxenite (trace element composition of mean N-MORB; Gale et al., 2013). The DMM and PM sources were modeled as hydrous peridotites with 110 ppm and 200 ppm of H_2O, respectively. That of DMM is based on the estimate of Workman & Hart (2005) and that of PM is the upper limit that permits the adiabat to intersect the solidus at 9 GPa, the highest pressure considered in REEBOX PRO. We note that although water contents up to >1000 ppm have been suggested for the primitive mantle reservoir (Palme & O'Neill, 2014), the preservation of volatiles in ancient mantle reservoirs, even if isolated from mantle convection, is uncertain. The hydrous melting functions of pyroxenites are poorly known, and there is no option to model wet pyroxenite in REEBOX PRO. The reason for choosing G2 over other pyroxenites available in REEBOX PRO (MIX1G and KG1) is that it contains the least garnet. This helps us to estimate the maximum amount of the pyroxenite component in creating garnet-absent HREE signatures in partial melts. This is also the reason for modeling two lithological mixtures: PM pyrolite and N-MORB G2 pyroxenite in proportions 99:1 (MIX-1) and 90:10 (MIX-2), respectively.

We selected a range of mantle potential temperatures, $T_p = 1350–1650°C$ (Fig. 2a), that conforms to the range of mean values recently suggested for 'coldspots' and hotspots by Bao et al. (2022) with a reference mid-ocean ridge adiabat of ~1380°C. The modeling was performed without a pre-existing lithosphere, but the 'lidless' output was mined for inspection for various lithospheric thicknesses by filtering the output data based on the estimated pressure at the lithosphere–asthenosphere boundary. We focus our inspection on lithospheric thicknesses (lid_t) of 150, 100 and 50 km (Fig. 2a). Assuming a crustal density of 2700 kg/m³, mantle density of 3300 kg/m³, and progressive thinning of the lithospheric mantle (crustal fractions of 0.3, 0.4, and 0.6, respectively), the corresponding pressures are 4.6, 3.0, and 1.4 Gpa. At the former two pressures, garnet is a stable phase at the solidus in all modeled sources.

Melt inclusion studies indicate that primitive CFB compositions result from mixing of instantaneous melts along the melting column and/or deep within the lithospheric plumbing system prior to eruption (e.g. Jennings et al., 2017). Therefore, we focus on the 'column-accumulated' melt outputs from REEBOX PRO in this study (Fig. 2b–c). For models containing mixtures of peridotite and pyroxenite, we calculate a combined column-accumulated melt composition by mixing their respective column-accumulated melts in the proportions these are present in the melting column using eq. 9 of Brown & Lesher (2016). Because we are interested in column-accumulated melt compositions, and not bulk crust properties, we did not need to assume a style of mantle flow for the models presented here. Finally, for modeling the trace element composition of the accumulated melts in the melting column, we used the default temperature-dependent partition coefficients for peridotite and static partition
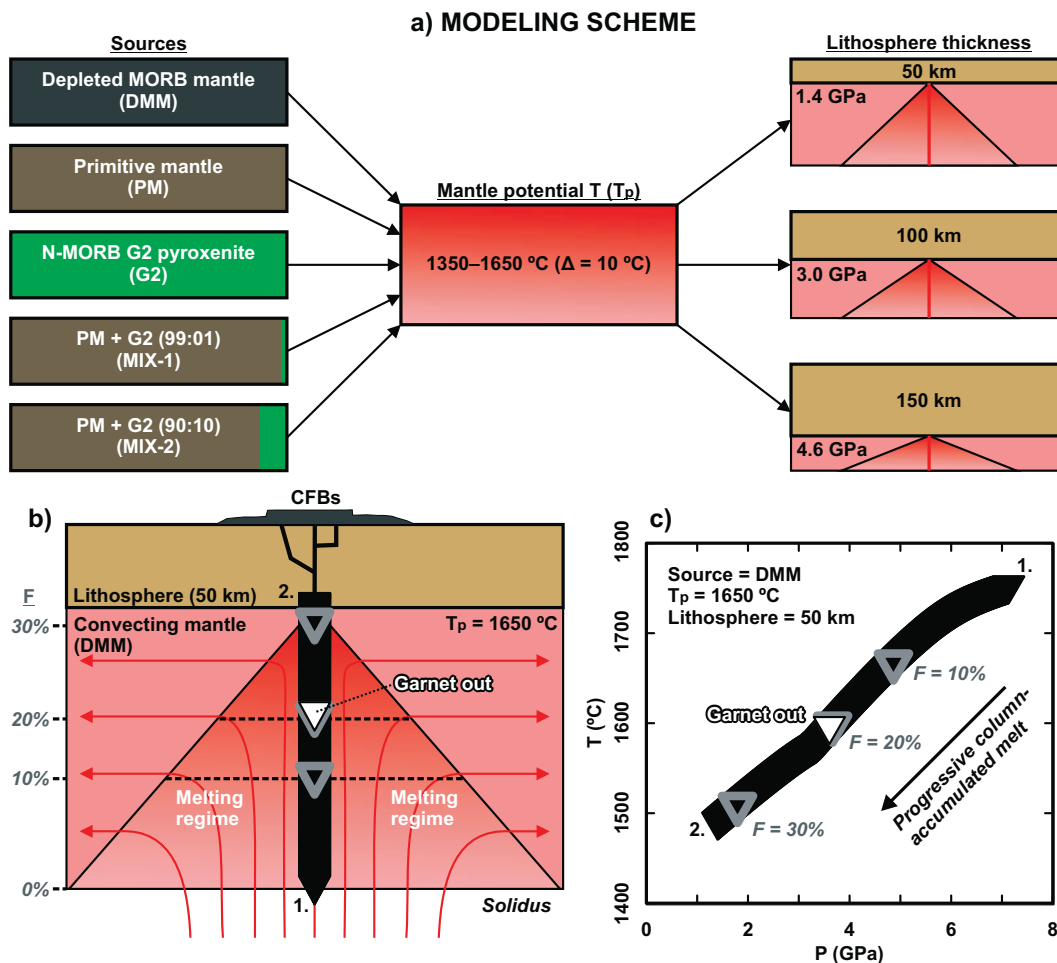
Figure 2. (a) The REEBOX PRO modeling scheme of this study. (b−c) Column-accumulated melting along the longest solid-mantle flow line through the melting regime illustrated in (b) a cross-section of lithosphere and convecting mantle (see Brown & Lesher, 2016) and (c) in a P vs. T diagram. The example is for the case of a depleted peridotite source, $T_p = 1650°C$, and lithospheric thickness of 50 km. The first instantaneous melt forms above the solidus at ~7.1 GPa (1.). Subsequent steps record progressive instantaneous melts that are mixed together in the melting column. The last instantaneous melt forms at the bottom of the lithosphere at 1.4 GPa (2.)—this point also represents the final column-accumulated melt, a mixture of all instantaneous melts formed above solidus T (from (1.) to (2.); eq. 8 in Brown & Lesher, 2016). Degrees of melting at 10% intervals are indicated with gray triangles. The point where garnet is exhausted from the residue is indicated with a white triangle.

coefficients for pyroxenite provided in REEBOX (see Brown & Lesher, 2016). We assumed default values for all other model parameters.

RESULTS

The results of the 155 simulations covering ~71 500 discrete P and T conditions are illustrated in Figs 3–8. In addition, selected results of the column-accumulated melts with lid_t of 150, 100, and 50 km are tabulated in Table 1. The full model outputs can be found as Supplementary Material.

The pressure vs. temperature plot (Fig. 3) illustrates the melting paths of the different sources as well as their different melting behaviors at varying lid_t. It is not surprising that, for a given T_p, the degree and pressure range of melting, i.e. the length of the melting path, increase with decreasing lid_t regardless of the mantle source. Also, the melting paths of fertile pyrolite (PM) are longer than those for depleted peridotite (DMM), given the difference in their solidi. The melt productivity of dry G2 pyroxenite is notably higher than that of the hydrous peridotite sources. This behavior is also reflected in the mixed sources: the shapes of the melting paths of MIX-1 and MIX-2 in PT-space are similar to that of PM,

but the total degrees of melting in the mixtures are higher at the same T_p. At high T_p values (~1500–1600°C), garnet is completely exhausted from all source residues for lid_t of 100 km, except for the case of pure G2 pyroxenite.

Rather than showing pressures, Fig. 4 illustrates the relationship between $(Dy/Yb)_N$ (see Fig. 1a, b) of the column-accumulated melts and temperature for the whole range of T_p. The relatively longer melting paths of simulations with lower lid_t (see Fig. 3) result in relatively larger variation in the HREE ratios in the melts. The results show that for a lid_t of 100 km, the range of Dy/Yb of the selected low-Ti and high-Ti CFBs can be generated by just varying the mantle source, degree of melting and T_p (see also Table 1). In fact, the lowest Dy/Yb values shown by the melts derived from the high-T_p (≥1600°C) peridotite simulations (DMM and PM) with $lid_t = 100$ km overlap with those of N-MORB and average low-Ti CFBs, despite garnet being initially present at the onset of melting in the model mantle source. In contrast, none of the melts with lid_t of 150 km reach such low values and only overlap with the high-Ti CFB magma compositions. At $lid_t > 100$ km, pure pyroxenite melts exhibit higher Dy/Yb than the majority of the Karoo CFBs, whether low Ti or high Ti (Fig. 4c). In addition, melts from the mixed source with 10% of pyroxenite (MIX-2) barely reach the low Dy/Yb of

Table 1: Selected results of the REEBOX PRO modeling for the final column-accumulated melts

	lid$_t$ = 150 km (P = 4.6 GPa)					lid$_t$ = 100 km (P = 3.0 GPa)					lid$_t$ = 50 km (P = 1.4 GPa)				
	DMM	PM	G2	MIX-1	MIX-2	DMM	PM	G2	MIX-1	MIX-2	DMM	PM	G2	MIX-1	MIX-2
T$_p$ = 1350°C															
F	-	-	-	-	-	-	0.46%	9.03%	0.64%	2.03%	7.24%	10.60%	35.70%	11.09%	15.29%
Garnet mode	-	-	-	-	-	-	2.01%	15.40%	2.08%	3.13%	0%	0%	4.23%	0%	0%
(Dy/Yb)$_N$	-	-	-	-	-	-	1.88	2.38	2.09	2.26	1.00	1.11	1.94	1.13	1.26
T$_p$ = 1400°C															
F	-	-	-	-	-	0.33%	2.30%	16.10%	2.62%	5.00%	12.50%	15.80%	42.10%	16.35%	20.75%
Garnet mode	-	-	-	-	-	2.11%	1.64%	14.10%	1.61%	2.50%	0%	0%	3.01%	0%	0%
(Dy/Yb)$_N$	-	-	-	-	-	1.59	1.84	2.33	1.91	2.10	0.99	1.09	1.89	1.11	1.18
T$_p$ = 1450°C															
F	-	0.06%	-	0.06%	0.05%	2.85%	6.19%	23.40%	6.53%	9.36%	17.00%	20.70%	48.10%	21.39%	25.57%
Garnet mode	-	12.10%	-	12.20%	13.13%	1.57%	0.84%	12.70%	0.93%	1.72%	0%	0%	1.85%	0%	0%
(Dy/Yb)$_N$	-	2.05	-	2.05	2.05	1.59	1.70	2.28	1.75	1.94	0.97	1.06	1.84	1.07	1.17
T$_p$ = 1500°C															
F	-	1.21%	4.65%	1.27%	1.78%	7.83%	11.40%	30.40%	11.83%	14.76%	20.70%	23.50%	53.40%	23.87%	29.17%
Garnet mode	-	11.60%	21.40%	11.69%	12.60%	0.47%	0%	11.30%	0.03%	0.64%	0%	0%	0.81%	0%	0%
(Dy/Yb)$_N$	-	1.97	2.60	2.05	2.34	1.43	1.45	2.23	1.51	1.78	0.95	1.03	1.79	1.06	1.18
T$_p$ = 1550°C															
F	1.35%	4.40%	11.70%	4.52%	5.58%	13.60%	16.90%	37.10%	17.33%	20.53%	24.20%	26.40%	58.40%	26.94%	31.69%
Garnet mode	11.60%	10.40%	19.80%	10.47%	11.31%	0%	0%	9.98%	0%	0.13%	0%	0%	0%	0%	0%
(Dy/Yb)$_N$	1.71	1.85	2.54	1.90	2.18	1.22	1.27	2.19	1.31	1.58	0.93	1.01	1.75	1.03	1.18
T$_p$ = 1600°C															
F	5.80%	9.60%	18.80%	9.74%	10.95%	19.50%	22.50%	43.10%	22.88%	26.15%	27.90%	29.90%	62.30%	30.21%	34.48%
Garnet mode	9.87%	8.39%	18.20%	8.50%	9.44%	0%	0%	8.85%	0%	0%	0%	0%	0%	0%	0%
(Dy/Yb)$_N$	1.58	1.69	2.48	1.73	1.98	1.08	1.15	2.16	1.18	1.40	0.90	0.99	1.72	1.01	1.18
T$_p$ = 1650°C															
F	11.90%	15.40%	25.90%	15.51%	16.89%	23.70%	26.50%	48.70%	26.84%	31.06%	31.90%	34.20%	64.60%	34.46%	37.72%
Garnet mode	7.52%	6.16%	16.60%	6.27%	7.33%	0%	0%	7.76%	0%	0%	0%	0%	0%	0%	0%
(Dy/Yb)$_N$	1.42	1.52	2.43	1.56	1.81	1.02	1.09	2.13	1.13	1.31	0.88	0.96	1.75	1.00	1.20

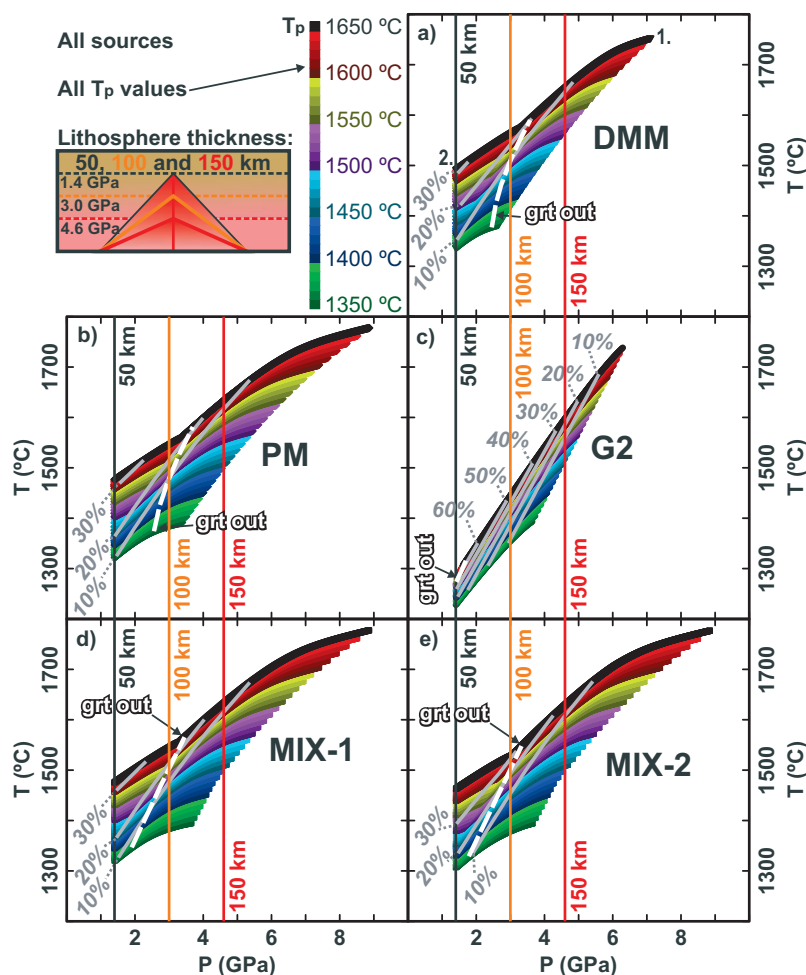F, degree of melting; Dy/Yb normalized to C1 chondrite (McDonough & Sun, 1995).

Figure 3. Column-accumulated partial melts of the different sources (a, depleted MORB mantle peridotite; b, primitive mantle peridotite; c, G2 pyroxenite; d, mixture of PM and G2 (99:1); e, mixture of PM and G2 (99:10)) modeled with REEBOX PRO illustrated as melting paths in P vs. T diagrams. Numbers (1.) and (2.) in (a) correspond to the ones shown in Fig. 2b and c (first instantaneous melt and final column-accumulated melt, respectively). T_p of the melting paths is indicated with a color palette from dark green ($T_p = 1350°C$) to black ($T_p = 1600°C$). Cutoff lines for lithospheric thicknesses of 150 and 100 km are indicated with red and orange lines, respectively—the whole model output represents the cutoff value for a lithospheric thickness of 50 km (vertical black line). In addition, degrees of melting (grey contours, percentages in italics) and the points where garnet is exhausted from the residue (white contours) are indicated (see Fig. 2b,c). The total degrees of melting for the mixtures have been calculated $F^{tot} = f_{PM}F_{PM} + f_{G2}F_{G2}$, where f is fraction of the component in the mixture.

low-Ti Karoo CFBs at $lid_t > 100$ km (Fig. 4e). Even with the smallest lid_t of 50 km, only the melts from sources containing less than 10% pyroxenite (DMM, PM, and MIX-1) reach the low Dy/Yb values of the low-Ti CFBs.

In Fig. 4, we only use elemental ratios of the model output in comparison to natural data. It is thus reasonable to test whether the elemental concentrations (including elements other than the REEs) in the model melts are consistent with the concentrations observed in CFBs. The simulations are shown in a Ti vs. Zr plot in Fig. 5, together with the wide selection of low-Ti and high-Ti Karoo CFB magma types. The simulations and the natural data show considerable overlap and thus suggest that, not only the ratios, but also the trace element concentrations in the modeled melts are reasonable. The implications of Figs 4 and 5 are further discussed in the following sections.

DISCUSSION
Constraints on the low-Ti vs. high-Ti classification of flood basalts

Bellieni *et al.* (1984) and Cox (1988) were among the first to suggest the division of flood basalts related to the Gondwana

break-up into low-Ti and high-Ti types. This classification scheme has subsequently spread and has been used in studies of other flood basalt provinces (e.g. Lightfoot *et al.,* 1993; Melluso *et al.,* 1995; Xu *et al.,* 2001; Shellnutt, 2014). There is no universally accepted principle of division, however, which hampers comparison between different provinces (see, e.g. Hou *et al.,* 2011). One of the underlying issues is that the designated low-Ti and high-Ti magma types generally show considerable overlap in terms of various geochemical characteristics (e.g. Hou *et al.,* 2011; Natali *et al.,* 2017; Luttinen, 2018).

The geochemical overlap and ambiguity in dividing flood basalts into low-Ti and high-Ti types also influences the interpretations of their origin. Although low-Ti and high-Ti flood basalts are generally thought to derive from distinct mantle sources, there are several obstacles in the way of such a straightforward interpretation. The degree and pressure of mantle melting and subsequent differentiation (fractional crystallization, assimilation) can significantly influence Ti contents and its ratios to other generally incompatible elements, and detailed research is often required to identify actual petrogenetically related melt assemblages (e.g. Hou *et al.,* 2011; Shellnutt & Jahn, 2011;
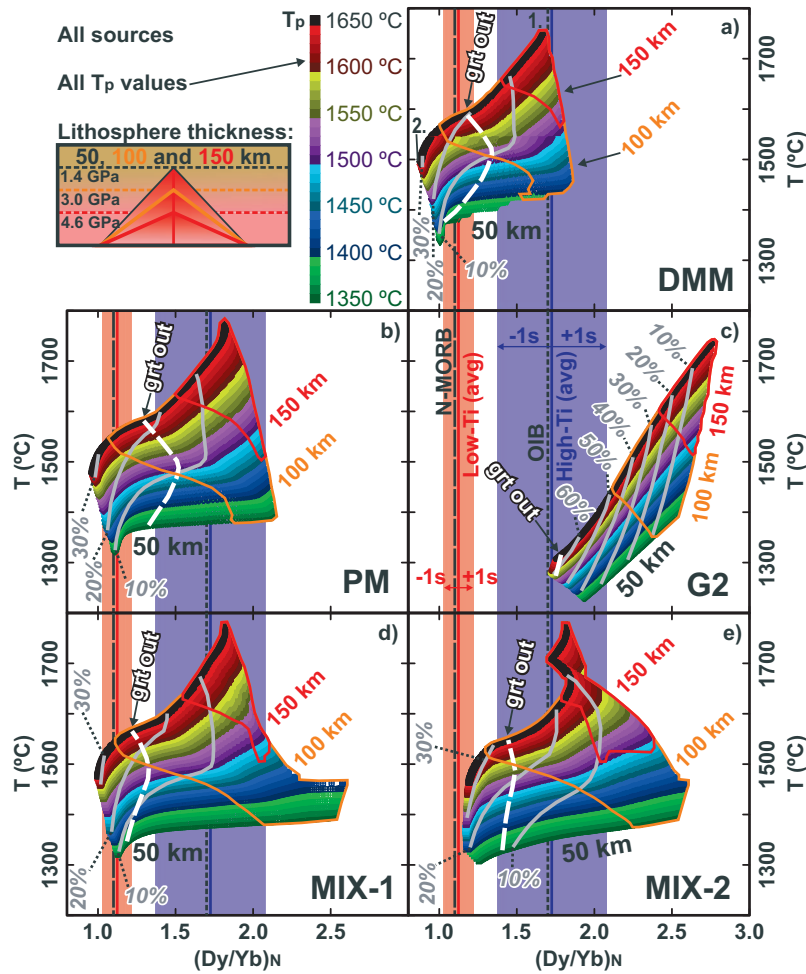
Figure 4. Column-accumulated partial melts of the different sources (a, depleted MORB mantle peridotite; b, primitive mantle peridotite; c, G2 pyroxenite; d, mixture of PM and G2 (99:1); e, mixture of PM and G2 (99:10)) modeled with REEBOX PRO illustrated as melting paths in $(Dy/Yb)_N$ vs. T diagrams. Numbers (1.) and (2.) in (a) correspond to the ones shown in Fig. 2b and c (first instantaneous melt and final column-accumulated melt, respectively). T_p of the melting paths is indicated with a color palette from dark green ($T_p = 1350°C$) to black ($T_p = 1600°C$). Cutoff lines for lithospheric thicknesses of 150 and 100 km are indicated with red and orange fields, respectively—the whole model output represents the cutoff value for a lithospheric thickness of 50 km. In addition, degrees of melting (grey contours, percentages in italics) and the points where garnet is exhausted from the residue (white contours), are indicated (see Fig. 2b,c). The vertical blue line indicates average $(Dy/Yb)_N$ of high-Ti Karoo Rift CFB and the vertical red line indicates average $(Dy/Yb)_N$ of low-Ti Karoo Basin CFB, with the respective fields showing ±1 s. Values for average OIB (Sun & McDonough, 1989) and mean N-MORB (Gale et al., 2013) are shown with vertical black stippled lines. These have $(Dy/Yb)_N$ values very close to average high-Ti and low-Ti CFBs, respectively. See Fig. 1 for data sources.

Natali *et al.*, 2017; Luttinen, 2018; Shellnutt & Pham, 2018; Zhang *et al.*, 2019). Our results illustrate this well: by varying the degree of melting of, for example, a pyrolitic source at a T_p of 1650°C, both high-Ti and low-Ti flood basalt magmas can be produced (Fig. 5b).

For the aforementioned reasons, we have only used selected flood basalt (and related dike and sill) data from the Karoo LIP for comparative purposes in Figs 1 and 4 in this study. The high-Ti and low-Ti Karoo magma types selected for these figures belong to the so-called Karoo Rift (conjugate African and Antarctic rifted margins and associated failed rifts) and Karoo Basin (main Karoo Basin, Kalahari Basin, and Zambezi Basin) sub-provinces, respectively. These correspond to the 'South Karoo' and 'North Karoo' sub-provinces of Luttinen (2018), but we favor the aforementioned names here to avoid mixing up with a historic geochemical North vs. South provincial scheme of Cox et al. (1967). The Karoo Rift and Basin sub-provinces have been interpreted on the basis of trace element (Nb, Zr, Y) and Nd and Sr isotope data to represent two major source areas—possibly upper mantle and plume,

respectively—in the sub-Gondwanan mantle (Luttinen, 2018). The low-Ti types that belong to the Karoo Rift sub-province, which were not included in Figs 1 and 4, clearly show higher Dy/Yb than the low-Ti types of the Karoo Basin sub-province (e.g. Fig. 6a), indicating a separate petrogenetic history as discussed in the following section.

Mantle sources of flood basalts—application to the Karoo LIP

The HREE concentrations of mantle partial melts modeled using REEBOX PRO with varying source composition, T_p and lid$_t$, provide valuable constraints for the origins of the natural samples. Figures 6−8 illustrate $(Dy/Yb)_N$ vs. Dy for a wide selection of low-Ti and high-Ti Karoo LIP magma types that have been filtered based on their petrogenetic relationships. In this section, we first briefly review the different magma types and then constrain their petrogenetic histories based on their HREE characteristics and previous geochronological, geochemical, and petrological research. For more information on the division of the low-Ti and high-Ti Karoo
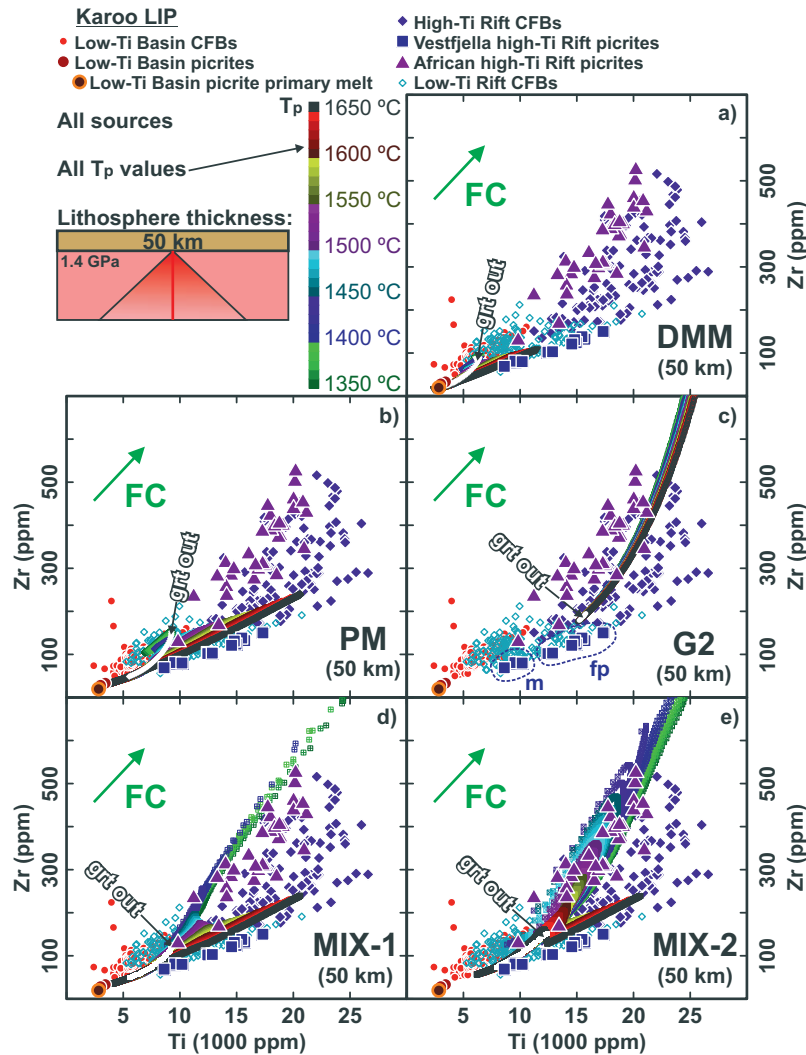
Figure 5. Column-accumulated partial melts of the different sources (a, depleted MORB mantle peridotite; b, primitive mantle peridotite; c, G2 pyroxenite; d, mixture of PM and G2 (99:1); e, mixture of PM and G2 (90:10)) modeled with REEBOX PRO illustrated as melting paths in Ti vs. Zr diagrams for lithospheric thickness of 50 km. T_p of the melting paths is indicated with a color palette from dark green ($T_p = 1350°C$) to black ($T_p = 1600°C$). The points where garnet is exhausted from the residue are indicated with white contours (see Fig. 2b–c), but degrees of melting are not shown to preserve clarity. The effect of fractional crystallization (FC) is approximated with a green arrow. Various Karoo LIP magma types are shown for reference; 'fp' and 'm' fields (only shown in c) indicate Vestfjella depleted ferropicrites and meimechites, respectively. The Karoo CFB data sources in addition to those mentioned in Fig. 1 are Ellam & Cox (1989, 1991), Harris *et al.* (1990), Luttinen & Furnes (2000), Riley *et al.* (2005), Heinonen & Luttinen (2008), Luttinen *et al.* (2010), Kamenetsky *et al.* (2017), and Turunen *et al.* (2019). For full data compilation, see Supplementary Data.

LIP magma types and their temporal and spatial distribution, the reader is referred to Luttinen (2018) and Turunen *et al.* (2019).

Review of the Karoo LIP magma types

The Karoo Rift magma types (color-coded blue-violet) can be divided into numerous high-Ti and low-Ti types that cover a wide age span (~190–178 Ma; Jourdan *et al.,* 2008; Moulin *et al.,* 2017; Luttinen *et al.,* 2022, and references therein; Fig. 1c). Both low-Ti and high-Ti types are geochemically diverse, typically of small volume, and related to the fossil rift system that developed into the conjugate rifted margins of Africa and Antarctica during Gondwana breakup (e.g. Burke & Dewey, 1973; Duncan *et al.,* 1984; Sweeney *et al.,* 1994; Luttinen *et al.,* 1998, 2010, 2015; Riley *et al.,* 2005; Manninen *et al.,* 2008; Luttinen, 2018, 2021). These Rift CFBs show evidence of lithospheric source components and likely sampled SCLM, subduction-modified upper mantle, and recycled mantle sources. Two of the most studied primitive examples have been selected for comparison in

this study: (1) the Vestfjella depleted ferropicrites and meimechites ('Vestfjella high-Ti Rift picrites' in Figs 5–8) typically have high-Ti compositions and have been suggested to represent low-degree partial melts from subduction-modified but otherwise long-term depleted upper mantle peridotite that was heated by supercontinent insulation, a mantle plume, or both (Heinonen *et al.,* 2010, 2018; Heinonen & Kurz, 2015); (2) the Mwenezi, Tuli, and Lebombo picrites ('African high-Ti Rift picrites' in Figs 5–8) represent a heterogeneous group of mostly primitive high-Ti magmas, likely derived from recycled pyroxenite-rich mantle sources that possibly represented enriched parts of Gondwanan SCLM (Harris *et al.,* 2015; Kamenetsky *et al.,* 2017).

The Karoo Basin magma types (color-coded orange-red) are all low-Ti. These are characterized by large magma volumes (e.g. extensive sill complexes in southern Africa), narrow age spans (183–182 Ma, the main Karoo pulse; Svensen *et al.,* 2012; Sell *et al.,* 2014; Greber *et al.,* 2020), and limited geochemical variation and are related to extensive sedimentary basins that
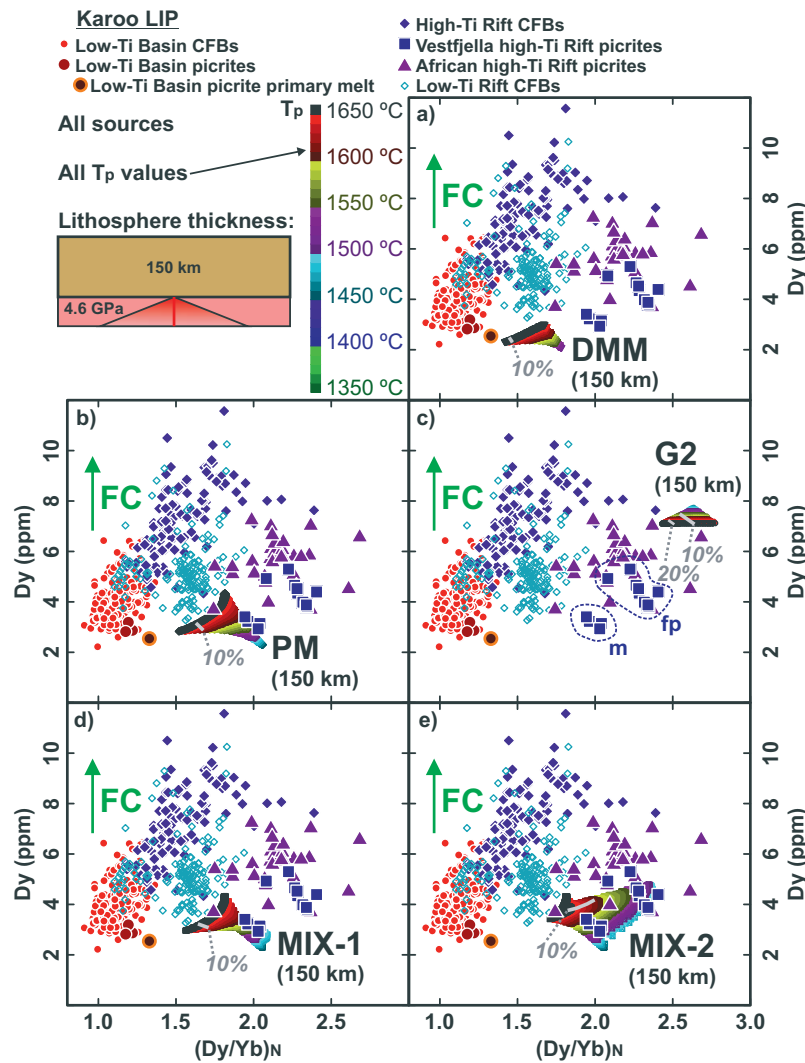
Figure 6. Column-accumulated partial melts of the different sources (a, depleted MORB mantle peridotite; b, primitive mantle peridotite; c, G2 pyroxenite; d, mixture of PM and G2 (99:1); e, mixture of PM and G2 (90:10)) modeled with REEBOX PRO illustrated as melting paths in $(Dy/Yb)_N$ vs. Dy diagrams for lithospheric thickness of 150 km. T_P of the melting paths is indicated with a color palette from dark green ($T_P = 1350°C$) to black ($T_P = 1600°C$). Degrees of melting (black contours, percentages in italics) are indicated (see Fig. 2b,c), but garnet is not exhausted from the source residue in any of the simulations. The effect of fractional crystallization (FC) is approximated with a green arrow. Various Karoo LIP magma types are shown for reference; 'fp' and 'm' fields (only shown in c) indicate Vestfjella depleted ferropicrites and meimechites, respectively. The Karoo CFB data sources listed in captions of Figs 1 and 5. For full data compilation, see Supplementary Data.

surround the main rift system (e.g. Duncan *et al.*, 1984; Marsh *et al.*, 1997; Jourdan *et al.*, 2007a; Neumann *et al.*, 2011; Luttinen, 2018; Fig. 1c). Primitive magma types belonging to this sub-province were not known until the discovery of low-Ti picrites from Luenha area, Zambezi Basin, Mozambique (Turunen *et al.*, 2019; 'low-Ti Basin picrites' in Figs 5—8). These picrites resemble the postulated parental magmas of the Basin sub-province (Luttinen, 2018) and have been suggested to derive from PM-like peridotite sources that were possibly entrained in a deep-derived mantle plume.

REEBOX PRO modeling and petrology of the Karoo LIP

In this section, we go forward with our comparison of the presented REEBOX PRO simulations and the Karoo LIP magma types following a simplified general scheme of progressive thinning of an initially 150-km thick lithosphere (lid_t). The comparisons are presented in $(Dy/Yb)_N$ vs. Dy space for lid_t of 150 km (Fig. 6), 100 km (Fig. 7), and 50 km (Fig. 8). Note that fractional crystallization increases Dy concentrations, but does not influence Dy/Yb

(Figs 6—8). Thus, the Dy concentrations of the uncontaminated and more primitive Karoo Rift magma types (Vestfjella and Africa) can be directly compared to the modeled melt compositions. Some of the non-cumulate low-Ti Basin picrites, however, are rather evolved (MgO < 10 wt%), so a parental melt composition calculated by Turunen *et al.* (2019) is also presented. In contrast, all the low-Ti and high-Ti CFBs and related intrusive rocks are rather evolved (MgO around 5–8 wt% on average) and their Dy concentrations must thus be higher than in their parental melts, which should be kept in mind when comparing with the model results (which reflect primary mantle melts).

Our modeling scenario starts during the initial stage of Karoo magmatism, with a lid_t of 150 km close to the typical values in the continental interior of southern Africa, except for the keel of the Kaapvaal craton (e.g. Globig *et al.*, 2016). Geochronological data suggest initial magmatism was associated with the Karoo Rift (Luttinen *et al.*, 2015, 2022). Specifically, the Vestfjella high-Ti Rift picrites and the low-Ti Rift CFBs have been dated at ~189–186 Ma
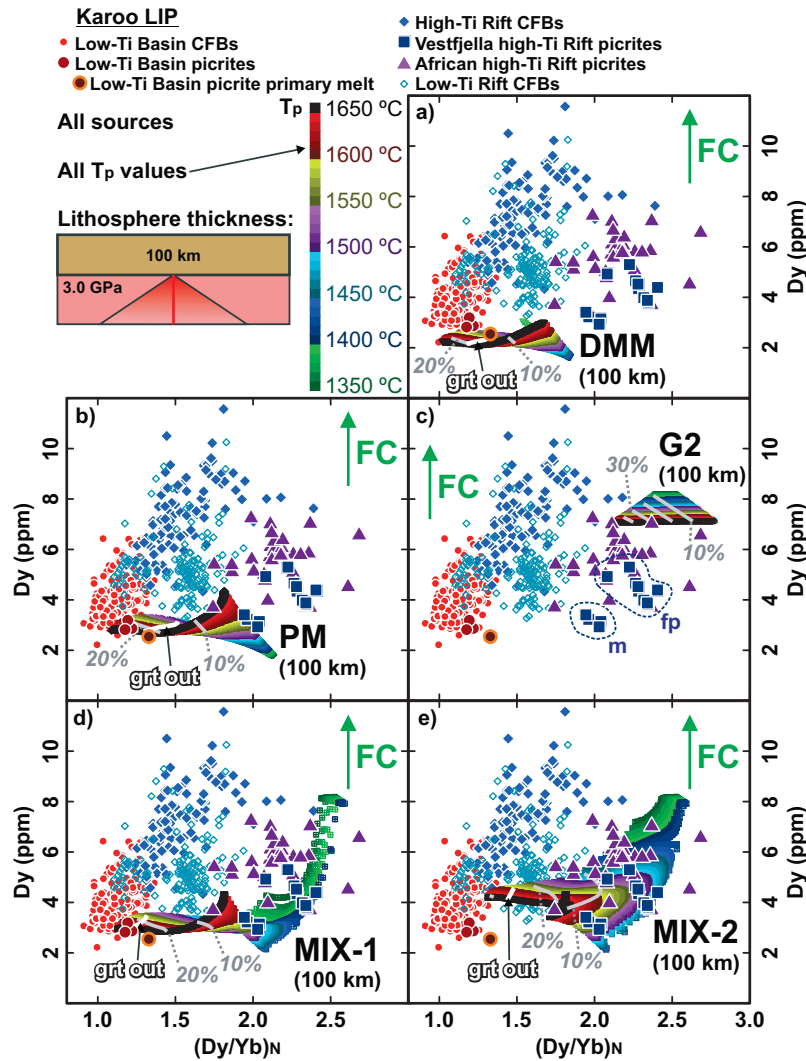
Figure 7. Column-accumulated partial melts of the different sources (a, depleted MORB mantle peridotite; b, primitive mantle peridotite; c, G2 pyroxenite; d, mixture of PM and G2 (99:1); e, mixture of PM and G2 (99:10)) modeled with REEBOX PRO illustrated as melting paths in $(Dy/Yb)_N$ vs. Dy diagrams for lithospheric thickness of 100 km. T_p of the melting paths is indicated with a color palette from dark green ($T_p = 1350°C$) to black ($T_p = 1600°C$). Degrees of melting (black contours, percentages in italics) and the points where garnet is exhausted from the residue (white contours) are indicated (see Fig. 2b,c). The effect of fractional crystallization (FC) is approximated with a green arrow. Various Karoo LIP magma types are shown for reference; 'fp' and 'm' fields (only shown in c) indicate Vestfjella depleted ferropicrites and meimechites, respectively. The Karoo CFB data sources listed in captions of Figs 1 and 5. For full data compilation, see Supplementary Data.

and seem to represent the earliest phase of Karoo magmatism (Luttinen *et al.,* 2015, 2022). Our modeling shows that these two Karoo magma types have HREE characteristics that could be explained by derivation beneath 150-km thick lithosphere (Fig. 6). The Vestfjella picrites could represent high-T ($T_p > 1500°C$) melting of fertile peridotitic sources with minor ($\leq 10\%$) pyroxenite (Fig. 6b, d, e). This fits well with what has been previously suggested for the meimechitic end-members of this group: $T_p > 1500–1600°C$, pressure of 5–6 GPa, degree of melting $\leq 10\%$, and only a minor entrainment of possible pyroxenite materials (Heinonen & Luttinen, 2010; Heinonen *et al.,* 2015, 2018; Heinonen & Fusswinkel, 2017). Compared to the meimechites, the ferropicrite compositions could represent either derivation at lower T_p, derivation from more pyroxenitic sources, or reflect lower degrees of melting at higher pressures (or all of these options; Fig. 6). The HREE characteristics of the low-Ti Rift CFBs could be explained by differentiation from dominantly high-pressure peridotite-derived melts (Fig. 6a, b, d). All the aforementioned implications are also

compatible with the Ti and Zr concentrations presented in Fig. 5. According to previous studies, the Vestfjella high-Ti Rift picrites and the low-Ti Rift CFBs were likely sourced from subduction-modified upper mantle that was heated by supercontinent insulation and/or a mantle plume (Heinonen *et al.,* 2010; Heinonen & Kurz, 2015; Luttinen, 2018, 2021). Our modeling as well as the available age data are compatible with a mantle plume closing in to the base of the thick continental lithosphere and heating and melting the upper mantle prior to the main pulse of Karoo magmatism. Substantial thinning of the lithosphere is not required at this stage.

The model results for lid_t of 100 km and 50 km (Figs 7–8) correspond to the main tectonomagmatic stage in the period ~184 Ma to ~178 Ma after rifting had produced regions of thinned lithosphere. This period encompasses two widespread pulses of voluminous magmatism at ~183–182 Ma and ~181–180 Ma, during which most of the African high-Ti and low-Ti picrites and basalts were generated (Luttinen *et al.,* 2022, and
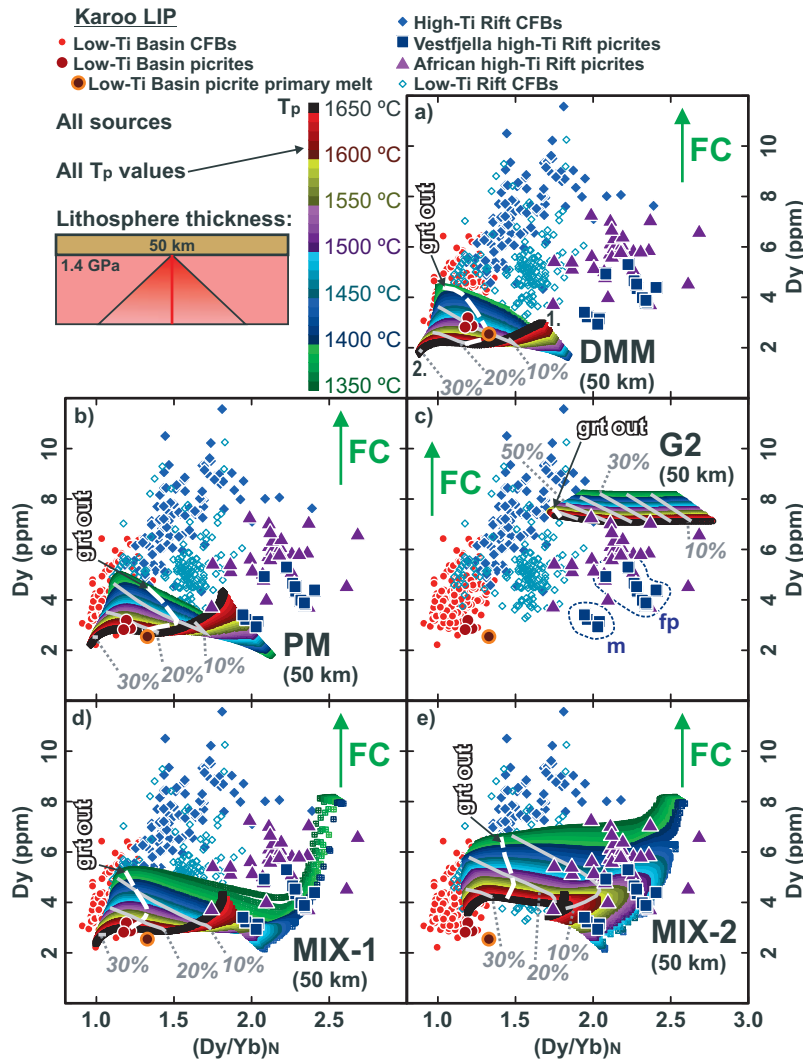
Figure 8. Column-accumulated partial melts of the different sources (a, depleted MORB mantle peridotite; b, primitive mantle peridotite; c, G2 pyroxenite; d, mixture of PM and G2 (99:1); e, mixture of PM and G2 (99:10)) modeled with REEBOX PRO illustrated as melting paths in $(Dy/Yb)_N$ vs. Dy diagrams for lithospheric thickness of 50 km. Numbers (1.) and (2.) in (a) correspond to the ones shown in Fig. 2b and c (first instantaneous melt and final column-accumulated melt, respectively). T_p of the melting paths is indicated with a color palette from dark green ($T_p = 1350°C$) to black ($T_p = 1600°C$). Degrees of melting (black contours, percentages in italics) and the points where garnet is exhausted from the residue (white contours) are indicated (see Fig. 2b,c). The effect of fractional crystallization (FC) is approximated with a green arrow. Various Karoo LIP magma types are shown for reference; 'fp' and 'm' fields (only shown in c) indicate Vestfjella depleted ferropicrites and meimechites, respectively. The Karoo CFB data sources listed in captions of Figs 1 and 5. For full data compilation, see Supplementary Data.

references therein). Judging from our models, the African high-Ti Rift picrites could have been generated from pyroxenite-rich (>10%) sources beneath a lid_t of 100 km (Fig. 7c, e; see also Fig 5c, e). Their generation could represent the impingement of the Karoo mantle plume on the sub-Gondwanan lithosphere (see Hu *et al.*, 2018; Celli *et al.*, 2020), which would have resulted in melting of fertile recycled materials preserved at the base of the lithospheric mantle (see Harris *et al.*, 2015; Kamenetsky *et al.*, 2017). Alternatively, these African high-Ti Rift picrites could represent melts from the fertile components inside the mantle plume. The three individual olivine crystals on which Sobolev *et al.* (2007) based their argument for 'almost pure pyroxenitic sources' for the entire Karoo LIP stem from this magma type. The ages of the African high-Ti Rift picrites have not been firmly established, but the available data and the related high-Ti basalt lavas and dikes constrain their age within ~184 Ma to ~179 Ma (e.g. Jourdan *et al.*, 2005, 2007b). Regarding the high-Ti Rift CFBs, many of their

Dy concentrations are very high and would require high degrees of fractional crystallization from primary melts generated at $lid_t = 100$ km (Fig. 7). This contradicts with their moderate Mg numbers, thus making this hypothesis unlikely. Instead, magma generation at lower pressures ($lid_t < 100$ km; Fig. 8) is suggested for these tholeiitic basalts. Thinner lithosphere is further compatible with their association mainly with the relatively younger 181–179 Ma pulse of the main period of Karoo magmatism (Luttinen *et al.*, 2022).

The compositions of low-Ti Karoo Basin magma types are suggestive of similar lithospheric thicknesses (≤100 km) to those suggested by the African high-Ti Rift picrites and CFBs. The low-Ti Basin picrites could represent high-T melting of peridotitic sources under $lid_t = 100$ km without major contribution from pyroxenite (Fig. 7a, b, d). Their flat HREE pattern (low Dy/Yb) would then record exhaustion or near-exhaustion of garnet from the mantle source at high degrees (≥20%) of melting. Again, this is
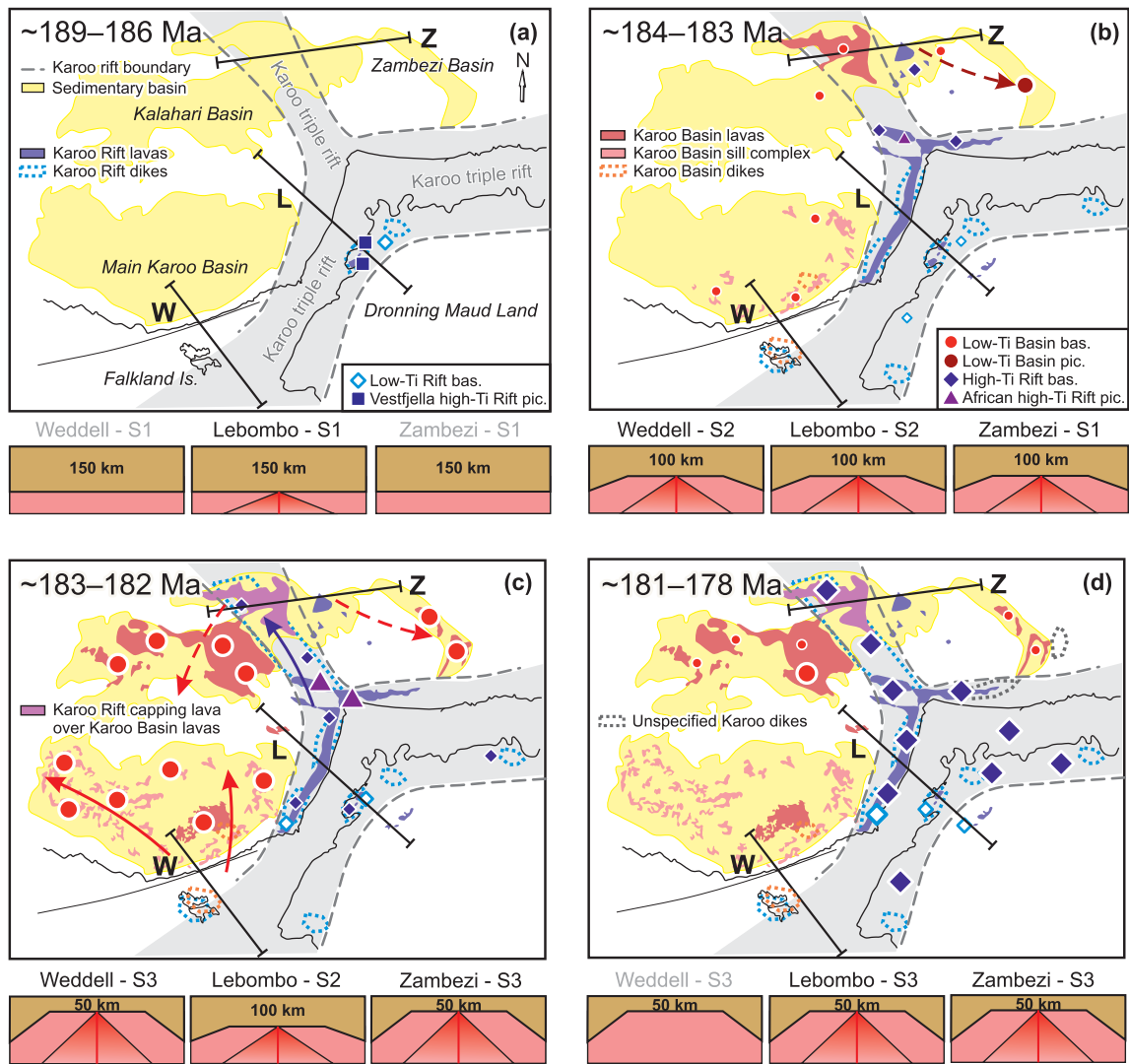
Figure 9. A simplified conceptual genetic scenario for Karoo LIP with different stages of progressive lithospheric thinning and associated magmatism as suggested by our modeling. The general distribution and geochemical affinities of Karoo CFBs and picrites (low-Ti and high-Ti Rift and low-Ti Basin magma types) formed during the (a) ~189–186 Ma, (b) ~184–183 Ma, (c) ~183–182 Ma, and (d) ~181–178 Ma phases of magmatism are schematically illustrated with the magma type symbol sizes reflecting the intensity and volume of magmatism. Differential lithospheric thinning through stages 1–3 (S1–S3; Figs 6–8) in different regions is shown across three cross-sections (W, Weddell Sea region; L, Lebombo Monocline region; Z, Zambezi region). In panels (b) and (c), the solid arrows depict previously proposed magma transportation patterns (Elliot & Fleming, 2000; Hastie *et al.*, 2014) and stippled arrows show magma transportation assumed in this study. We emphasize that this scenario is indefinite due to limitations of rock exposure and available geological, geochemical, and chronological data, and the uncertain locations of magma generation. See text for more information and Fig. 1c for detailed explanation of the map.

in line with what has been suggested earlier for the generation of their primary melts: pressure of 3–4 GPa, liquidus temperatures up to 1580°C at 3.5 GPa, and ~20% of partial melting of a dominantly peridotitic source resembling primitive mantle pyrolite (Turunen *et al.*, 2019). In comparison, most low-Ti Basin CFBs have Dy/Yb values that are consistent with a lid$_t$ of <100 km, unless they were derived from a depleted mantle peridotite source (Fig. 7). A depleted source is highly unlikely, however, given that the initial ε_{Nd} values of the least-contaminated samples are close to chondritic (+1.4; Riley *et al.*, 2005; Turunen *et al.*, 2019) and because their trace element characteristics point to undepleted sources (see Luttinen, 2018). The low-Ti Basin picrites have not been dated, which renders the geochemical evolution of low-Ti magmatism uncertain. Nevertheless, their formation must have taken place between ~188 Ma and 180 Ma (Luttinen *et al.*, 2022), allowing a scenario of progressive lithospheric thinning in which

the low-Ti picrites represent an initial phase and the ~183–182 Ma low-Ti CFBs represent the main phase of Basin magmatism.

We maintain that the generation of most Karoo Basin and Rift CFBs and related sills and dikes was likely related to areas of thinned, but still relatively thick, lithosphere during the main stage of magmatism ~184–178 Ma: the voluminous and homogeneous low-Ti Basin sub-province was likely generated primarily from peridotitic sources, and the less voluminous and heterogeneous high-Ti members of the Rift sub-province from more pyroxenite-rich sources (Fig. 8). Subsequent differentiation in crustal magma chambers contributed to the observed diversity in both types.

A schematic model for the Karoo LIP

Here we present a schematic model in order to provide a plausible geological framework for our results. The development of

a detailed 4D model of the tectonic and magmatic activity is presently precluded by the shortage of reliable age data for the Rift sub-province (Luttinen *et al.,* 2022) and the unknown locations of magma source regions for the Basin sub-province (e.g. Coetzee & Kristers, 2020) in particular. Our model postulates three distinctive main source regions for the Karoo magmas: (1) We consider that magmas in the Rift sub-province probably formed under the developing Africa-Antarctica rift system. Magma flow directions indicate broadly westward transportation of high-Ti Rift magmas in the Okavango dike swarm from the magma generation regions in this rift system (Hastie *et al.,* 2014). (2) The source areas of the basin CFBs are controversial, largely due to the apparent absence of crosscutting mafic dike swarms in the Precambrian basement of the Main Karoo Basin (e.g. Coetzee and Kisters, 2020). This suggests that significant crustal extension and rifting did not take place in the Main Karoo Basin and lends support to lateral transportation of magmas from source regions outside the basin, for example, in the proto Weddell Sea at the juncture of the African, Antarctic, and South American lithospheric plates (Elliot & Fleming, 2000). Bearing in mind the present >100 km lithospheric thickness in the Main Karoo Basin (Artemieva & Vinnik, 2016; Globig *et al.,* 2016), we favor the proto Weddell Sea area as the source region of the Main Karoo Basin CFBs. (3) The source regions of the Kalahari Basin CFBs are even more uncertain and have not been previously addressed. We tentatively identify the areas of exceptionally thin (<35 km) crust in the Kalahari Basin (e.g. at the juncture of the Okavango dike swarm; Fadel *et al.,* 2018) as a feasible location of Karoo-age rifting and generation of the Kalahari Basin CFBs.

The model assumes a uniform initial lithospheric thickness of 150 km (extensional stage 1) across the Karoo LIP at the onset of magmatism at ~189–186 Ma (Fig. 9a). We associate the earliest period of magmatism with initial melting of the heated and subduction-modified upper mantle above an ascending plume head before significant lithospheric thinning. The plume head may well have induced lithospheric up-doming and associated rifting along existing zones of weakness in the lithosphere (see Jourdan *et al.,* 2006). Examples of this phase are associated with the Rift sub-province and include the generation of early low-Ti Rift CFBs and Vestfjella high-Ti picrites and possibly other low-volume picritic, nephelinitic, and felsic Karoo magma types not considered in detail in this study (e.g. Bristow, 1984; Riley *et al.,* 2005; Heinonen *et al.,* 2010; Luttinen *et al.,* 2022).

Magmatism became more widespread at ~184–183 Ma due to initial melting of the plume head and thinning of the lithosphere in all three source regions (extensional stage 2; lid_t = 100 km; Fig. 9b). Examples of this period are associated with both sub-provinces and include the generation of African high-Ti Rift picrites and low-Ti Basin picrites, as well as some more evolved CFBs from both sub-provinces.

The climactic phase of Karoo magmatism at ~183–182 Ma was related to increased production of Basin CFBs in response to further thinning of the lithosphere in the source regions (extensional stage 3; lid_t < 100 km) (Fig. 9c). Judging from the geochemical and age data of the Rift magmas (e.g. 182 Ma low-Ti Rift gabbros/CFBs in Vestfjella; Luttinen *et al.,* 2015), the regions of advanced extension were limited to the Basin sub-province during this phase and the generation of Rift CFBs continued under relatively thick lithosphere (extensional stage 2: lid_t = 100 km).

The Rift magmatism peaked at ~181–178 Ma. We envisage that the very widespread production of high-Ti Rift CFBs (Luttinen *et al.,* 2022) was related to rapid lithospheric extension in the Africa–Antarctica rift (extensional stage 3; lid_t < 100 km) (Fig. 9d).

Low-Ti CFBs were also generated during this phase in the Kalahari Basin. Subsequently, magmatism in the Karoo LIP waned and the 178–162 Ma emplacement ages of localized mafic and silicic magmatism (Luttinen *et al.,* 2002, 2022; Jourdan *et al.,* 2007; Greber *et al.,* 2020) and 173–142 Ma alteration ages of CFBs (Zhang *et al.,* 2003; Luttinen *et al.,* 2015) record the development of a volcanic rifted margin—these later phases are not considered in our modeling.

The presented model illustrates that the different extensional stages probably took place at different times in different parts of the Karoo LIP (Fig. 9). We also point out that the model is based on stepwise modeling of a thinning lithosphere and should not be considered as a definitive evolutionary model for Karoo LIP magmatism in general. Nevertheless, the relative commonness and compositional diversity of primitive magma types related to the earliest 189–183 Ma phases (Fig. 9a, b) could be linked to their origin before notable lithospheric thinning and establishment of large and widespread central magma chambers (see Klausen, 2009). In comparison, the two widespread and voluminous pulses of low-Ti and high-Ti magmatism at ~183–178 Ma (Fig. 9c, d) are readily associated with a successive development of notably thinned regions of lithosphere in the Basin and Rift sub-provinces, respectively. During these magmatic peaks, the Gondwana lithosphere had thinned (its base still within garnet stability field) above the centers of magmatism, and the magmas differentiated to basaltic compositions in large central magma chambers. Finally, we emphasize that high mantle temperatures are a prerequisite for the presented scenario (Figs 6–8).

General implications for the petrogenesis of flood basalts

Our modeling is not only relevant for the Karoo LIP, but also raises several important points regarding the origin of CFBs globally. HREE patterns have generally been considered as indicators of the depth of mantle melting, but the presented modeling results clearly show that temperature (and thus degree of melting) and source composition have at least an equally, if not more, significant role in controlling HREE in CFB magmas (Figs 6–8). Our findings that have general relevance to CFB research are listed as follows:

1) Low-Ti CFBs cannot be generated from sources that contain more than ~10% pyroxenite in general (Figs 6–8). We emphasize that although we used mean N-MORB of Gale *et al.* (2013) as the trace element composition of the G2 pyroxenite, the use of more enriched compositions (e.g. E-MORB or continental crust) would be expected to result in even more drastic enrichment in Dy/Yb because of higher HREE concentrations and/or higher Dy/Yb than in N-MORB. In addition, G2 pyroxenite shows the lowest stability for garnet in relation to other pyroxenites for which phase equilibria are relatively well known (see Brown & Lesher, 2016). Therefore, the upper limits for pyroxenite involvement can indeed be constrained.

2) Low-Ti CFBs with flat HREE patterns can be generated from asthenospheric garnet peridotite sources at lithospheric thicknesses of ~100 km, but this requires high mantle temperatures (T_p > 1500°C) to consume garnet from the source. Thus, unlike previously speculated, the absence of a so-called 'garnet fingerprint' is not a definite indicator of a shallow melting origin of a given volcanic rock in hotspot environments. We emphasize that this does not mean that *all* low-Ti CFBs with flat HREE originate at such

conditions in the asthenospheric mantle. Our models do not exclude magma input from lithospheric sources. For example, the low-Ti and flat-HREE CFBs of the Panjal Traps in India are probably related to shallow melting of the lithospheric mantle during rifting and under ambient mantle temperatures (e.g. Shellnutt *et al.,* 2014; compare to Fig. 8). The sources have to be constrained individually for different settings and using several additional (e.g. isotopic) methods.

3) High-Ti CFBs derive dominantly from pyroxenite-bearing sources (Figs 6–8). Contrary to a common view, high-Ti CFBs with steep HREE patterns may form at similar pressures (and temperatures) as low-Ti CFBs with flat HREE patterns (Fig. 8). This is because residual garnet is far more stable in pyroxenite than peridotite sources.

4) Basalts having pyroxenite and peridotite sources coexist in CFB provinces, but need to be identified and dealt with separately in petrogenetic interpretations. For example, one might not get trustworthy temperature estimates for primitive magmas derived from pyroxenite-bearing sources using tools calibrated for purely peridotite-sourced melts (e.g. PRIMELT series algorithms; Herzberg & Asimow, 2015; see, e.g. Hole, 2015; Natali *et al.,* 2017).

Finally, we emphasize that these generalized outcomes should always be evaluated in the light of the CFB province in question and against other geochemical parameters. Nevertheless, HREE contents and their modeling with REEBOX PRO show great promise in placing constraints on the origin of various high- and low-Ti CFB parental magmas.

CONCLUSIONS

We modeled the HREE and other incompatible trace element contents of silicate melts formed by partial melting of depleted peridotite, pyrolitic peridotite, pyroxenite, and pyrolite-pyroxenite mixtures under varying mantle potential temperature and lithospheric thickness. The modeling was performed using the REEBOX PRO program (Brown & Lesher, 2016), which simulates adiabatic decompression melting using constraints from thermodynamics and melting experiments. The results of the modeling show that low-Ti CFBs with flat MORB-like HREE patterns originate from peridotite-dominated ($\geq$90%) sources and can be generated at elevated mantle temperatures beneath a lithosphere that is ~100 km thick. These magmas are thus not necessarily derived from a shallow spinel peridotite source alone. In contrast, high-Ti CFBs with steep OIB-like HREE patterns originate largely from pyroxenite-rich ($\geq$10%) sources and can also be generated beneath a considerably thinned (~50 km) lithosphere. Both magma types can thus be generated at similar mantle pressures, if mantle temperature (and thus degree of melting) and source composition is varied. These general constraints conform to previous studies on various low-Ti and high-Ti magma types of the Karoo LIP and paint a picture of progressive impingement of a mantle plume on the base of the lithosphere. The earliest primitive high-Ti magmas and some low-Ti magmas were generated beneath a thick continental lithosphere when the plume was still approaching. In contrast, the voluminous low-Ti and high-Ti magmas related to the main pulses at ~183–178 Ma were generated from peridotite and pyroxenite-bearing sources, respectively, after considerable thinning of the Gondwana lithosphere.

References

Artemieva, I. M. & Vinnik, L. P. (2016). Density structure of the Cratonic Mantle in Southern Africa: 1. Implications for dynamic topography. *Gondwana Research* **39**, 204–216. 10.1016/j.gr.2016.03.002.

Bao, X., Lithgow-Bertelloni, C. R., Jackson, M. G. & Romanow-icz, B. (2022). On the relative temperatures of Earth's volcanic hotspots and mid-ocean ridges. *Science* **375**, 57–61. 10.1126/science.abj8944.

Bellieni, G., Comin-Chiramonti, P., Marques, L. S., Melfi, A. J., Piccirillo, E. M., Nardy, A. J. R. & Roisenberg, A. (1984). High- and low-TiO₂ flood basalts from the Paraná Plateau (Brazil): petrology and geochemical aspects bearing on their mantle origin. *Neues Jahrbuch für Mineralogie Abhang* **150**, 273–306.

Bristow, J. W. (1984). Nephelinites of the north Lebombo and southeast Zimbabwe. In: Erlank, A.J. (ed.) *Petrogenesis of the Volcanic Rocks of the Karoo Province.* The Geological Society of South Africa Special Publication 13. The Geological Society of South Africa, Johannesburg, South Africa, 87–104.

Brown, E. L. & Lesher, C. E. (2016). REEBOX PRO: a forward model simulating melting of thermally and lithologically variable upwelling mantle. *Geochemistry, Geophysics, Geosystems* **17**, 3929–3968. 10.1002/2016GC006579.

Brown, E. L., Petersen, K. D. & Lesher, C. E. (2020). Markov chain Monte Carlo inversion of mantle temperature and source composition, with application to Reykjanes Peninsula, Iceland. *Earth and Planetary Science Letters* **532**, 116007, 1–15. 10.1016/j.epsl.2019.116007.

Bryan, S. E. & Ernst, R. E. (2008). Revised definition of large igneous provinces (LIPs). *Earth-Science Reviews* **86**, 175–202. 10.1016/j.earscirev.2007.08.008.

Bryan, S. E., Peate, I. U., Peate, D. W., Self, S., Jerram, D. A., Mawby, M. R., Marsh, J. S. & Miller, J. A. (2010). The largest volcanic eruptions on Earth. *Earth-Science Reviews* **102**, 207–229. 10.1016/j.earscirev.2010.07.001.

Burke, K. & Dewey, J. F. (1973). Plume-generated triple junctions: key indicators in applying plate tectonics to old rocks. *Journal of Geology* **81**, 406–433. 10.1086/627882.

Celli, N. L., Lebedev, S., Schaeffer, A. J. & Gaina, C. (2020). African cratonic lithosphere carved by mantle plumes. *Nature Communications* **11**, 92. 10.1038/s41467-019-13871-2.

Coetzee, A. & Kisters, A. F. M. (2020). Spatial variations of sills and implications for magma dispersal across the Karoo basin. *South African Journal of Geology* **123**, 511–530. 10.25131/sajg.123.0035.

Cox, K. G. (1988). The Karoo province. In: MacDougall, J. D. (ed.) *Continental Flood Basalts.* Dordrecht: Kluwer Academic Publishers, 239–271, 10.1007/978-94-015-7805-9_7.

Cox, K. G., MacDonald, R. & Hornung, G. (1967). Geochemical and petrographic provinces in the Karoo basalts of Southern Africa. *American Mineralogist* **52**, 145l–1471l.

Dasgupta, R., Jackson, M. G. & Lee, C.-T. A. (2010). Major element chemistry of ocean island basalts—conditions of mantle melting and heterogeneity of mantle source. *Earth and Planetary Science Letters* **289**, 377–392. 10.1016/j.epsl.2009.11.027.

Duncan, A. R., Erlank, A. J. & Marsh, J. S. (1984). Geochemistry of the Karoo igneous province. In: Erlank, A.J. (ed.) *Petrogenesis of the Volcanic Rocks of the Karoo Province.* The Geological Society of South Africa Special Publication 13. The Geological Society of South Africa, Johannesburg, South Africa, 355–388.

Ellam, R. M. & Cox, K. G. (1989). A Proterozoic lithospheric source for Karoo magmatism: evidence from the Nuanetsi picrites. *Earth and Planetary Science Letters* **92**, 207–218. 10.1016/0012-821X(89)90047-2.

Ellam, R. M. & Cox, K. G. (1991). An interpretation of Karoo picrite basalts in terms of interaction between asthenospheric magmas and the mantle lithosphere. *Earth and Planetary Science Letters* **105**, 330–342. 10.1016/0012-821X(91)90141-4.

Elliot, D. H. & Fleming, T. H. (2000). Weddell triple junction: the principal focus of Ferrar and Karoo magmatism during initial breakup of Gondwana. *Geology* **28**, 539–542. 10.1130/0091-7613(2000)28<539:WTJTPF>2.0.CO;2.

Fadel, I., van der Meijde, M. & Paulssen, H. (2018). Crustal structure and dynamics of Botswana. *Journal of Geophysical Research: Solid Earth* **123**, 10,659–10,671. 10.1029/2018JB016190.

Fujii, T. (1989). Genesis of mid-ocean ridge basalts. In: Saunders, A. D. & Norry, M. J. (eds.) *Magmatism in the Ocean Basins.* Geological Society Special Publication 42. The Geological Society, Blackwell Scientific Publications, Oxford, United Kingdom, 137–146, 10.1144/GSL.SP.1989.042.01.09.

Gale, A., Dalton, C. A., Langmuir, C. H., Su, Y. & Schilling, J. -G. (2013). The mean composition of ocean ridge basalts. *Geochemistry, Geophysics, Geosystems* **14**, 489–518. 10.1029/2012GC004334.

Galerne, C. Y., Neumann, E. -R. & Planke, S. (2008). Emplacement mechanisms of sill complexes: information from the geochemical architecture of the Golden Valley Sill Complex, South Africa. *Journal of Volcanology and Geothermal Research* **177**, 425–440. 10.1016/j.jvolgeores.2008.06.004.

Globig, J., Fernàndez, M., Torne, M., Vergés, J., Robert, A. & Faccenna, C. (2016). New insights into the crust and lithospheric mantle structure of Africa from elevation, geoid, and thermal analysis. *Journal of Geophysical Research: Solid Earth* **121**, 5389–5424. 10.1002/2016JB012972.

Greber, N. D., Davies, J. H. F. L., Gaynor, S. P., Jourdan, F., Bertrand, H. & Schaltegger, U. (2020). New high precision U-Pb ages and Hf isotope data from the Karoo large igneous province; implications for pulsed magmatism and early Toarcian environmental perturbations. *Results in Geochemistry* **1**, 100005. 10.1016/j.ringeo.2020.100005.

Harris, C., Marsh, J. S., Duncan, A. R. & Erlank, A. J. (1990). The petrogenesis of the Kirwan Basalts of Dronning Maud Land, Antarctica. *Journal of Petrology* **31**, 341–369. 10.1093/petrology/31.2.341.

Harris, C., le Roux, P., Cochrane, R., Martin, L., Duncan, A. R., Marsh, J. S., le Roex, A. P. & Class, C. (2015). The oxygen isotope composition of Karoo and Etendeka picrites: high δ^{18}O mantle or crustal contamination? *Contributions to Mineralogy and Petrology* **170**, 8. 10.1007/s00410-015-1164-1.

Hastie, W. W., Watkeys, M. K. & Aubourg, C. (2014). Magma flow in dyke swarms of the Karoo LIP: implications for the mantle plume hypothesis. *Gondwana Research* **25**, 736–755. 10.1016/j.gr.2013.08.010.

Heinonen, J. S. & Fusswinkel, T. (2017). High Ni and low Mn/Fe in olivine phenocrysts of the Karoo meimechites do not reflect pyroxenitic mantle sources. *Chemical Geology* **467**, 134–142. 10.1016/j.chemgeo.2017.08.002.

Heinonen, J. S. & Kurz, M. D. (2015). Low-^{3}He/^{4}He sublithospheric mantle source for the most magnesian magmas of the Karoo large igneous province. *Earth and Planetary Science Letters* **426**, 305–315. 10.1016/j.epsl.2015.06.030.

Heinonen, J. S. & Luttinen, A. V. (2008). Jurassic dikes of Vestfjella, western Dronning Maud Land, Antarctica: geochemical tracing of ferropicrite sources. *Lithos* **105**, 347–364. 10.1016/j.lithos.2008.05.010.

Heinonen, J. S. & Luttinen, A. V. (2010). Mineral chemical evidence for extremely magnesian subalkaline melts from the Antarctic extension of the Karoo large igneous province. *Mineralogy and Petrology* **99**, 201–217. 10.1007/s00710-010-0115-9.

Heinonen, J. S., Carlson, R. W. & Luttinen, A. V. (2010). Isotopic (Sr, Nd, Pb, and Os) composition of highly magnesian dikes of Vestfjella, western Dronning Maud Land, Antarctica: a key to the origins of the Jurassic Karoo large igneous province? *Chemical Geology* **277**, 227–244. 10.1016/j.chemgeo.2010.08.004.

Heinonen, J. S., Jennings, E. S. & Riley, T. R. (2015). Crystallisation temperatures of the most Mg-rich magmas of the Karoo LIP on the basis of Al-in-olivine thermometry. *Chemical Geology* **411**, 26–35. 10.1016/j.chemgeo.2015.06.015.

Heinonen, J. S., Luttinen, A. V. & Whitehouse, M. J. (2018). Enrichment of ^{18}O in the mantle sources of the Antarctic portion of the Karoo large igneous province. *Contributions to Mineralogy and Petrology* **173**, 21. 10.1007/s00410-018-1447-4.

Herzberg, C. (2006). Petrology and thermal structure of the Hawaiian plume from Mauna Kea volcano. *Nature* **444**, 605–609. 10.1038/nature05254.

Herzberg, C. & Asimow, P. D. (2015). PRIMELT3 MEGA.XLSM software for primary magma calculation: peridotite primary magma MgO contents from the liquidus to the solidus. *Geochemistry, Geophysics, Geosystems* **16**, 563–578. 10.1002/2014GC005631.

Hole, M. J. (2015). The generation of continental flood basalts by decompression melting of internally heated mantle. *Geology* **43**, 311–314. 10.1130/G36442.1.

Hou, T., Zhang, Z., Kusky, T., Du, Y., Liu, J. & Zhao, Z. (2011). A reappraisal of the high-Ti and low-Ti classification of basalts and petrogenetic linkage between basalts and mafic–ultramafic intrusions in the Emeishan Large Igneous Province, SW China. *Ore Geology Reviews* **41**, 133–143. 10.1016/j.oregeorev.2011.07.005.

Hu, J., Liu, L., Faccenda, M., Zhou, Q., Fischer, K. M., Marshak, S. & Lundstrom, C. (2018). Modification of the Western Gondwana craton by plume–lithosphere interaction. *Nature Geoscience* **11**, 203–210. 10.1038/s41561-018-0064-1.

Janoušek, V., Farrow, C. M. & Erban, V. (2006). Interpretation of whole-rock geochemical data in igneous geochemistry: introducing geochemical data toolkit (GCDkit). *Journal of Petrology* **47**, 1255–1259. 10.1093/petrology/egl013.

Jennings, E. S., Gibson, S. A., Maclennan, J. & Heinonen, J. S. (2017). Deep mixing of mantle melts beneath continental flood basalt provinces: constraints from olivine-hosted melt inclusions in primitive magmas. *Geochimica et Cosmochimica Acta* **196**, 36–57. 10.1016/j.gca.2016.09.015.

Jourdan, F., Féraud, G., Bertrand, H., Kampunzu, A. B., Tshoso, G., Watkeys, M. K. & Le Gall, B. (2005). The Karoo large igneous province: brevity, origin, and relation with mass extinction questioned by new ^{40}Ar/^{39}Ar age data. *Geology* **33**, 745–748. 10.1130/G21632.1.

Jourdan, F., Féraud, G., Bertrand, H., Watkeys, M. K., Kampunzu, A. B. & Le Gall, B. (2006). Basement control on dyke distribution in large igneous provinces: case study of the Karoo

triple junction. *Earth and Planetary Science Letters* **241**, 307–322. 10.1016/j.epsl.2005.10.003.

Jourdan, F., Bertrand, H., Schaerer, U., Blichert-Toft, J., Féraud, G. & Kampunzu, A. B. (2007a). Major and trace element and Sr, Nd, Hf, and Pb isotope compositions of the Karoo large igneous province, Botswana-Zimbabwe: lithosphere vs mantle plume contribution. *Journal of Petrology* **48**, 1043–1077. 10.1093/petrology/egm010.

Jourdan, F., Féraud, G., Bertrand, H., Watkeys, M. K. & Renne, P. R. (2007b). Distinct brief major events in the Karoo large igneous province clarified by new $^{40}Ar/^{39}Ar$ ages on the Lesotho basalts. *Lithos* **98**, 195–209. 10.1016/j.lithos.2007.03.002.

Jourdan, F., Féraud, G., Bertrand, H., Watkeys, M. K. & Renne, P. R. (2008). The $^{40}Ar/^{39}Ar$ ages of the sill complex of the Karoo large igneous province: implications for the Pliensbachian-Toarcian climate change. *Geochemistry, Geophysics, Geosystems* **9**, Q06009. 10.1029/2008GC001994.

Kamenetsky, V. S., Maas, R., Kamenetsky, M. B., Yaxley, G. M., Ehrig, K., Zellmer, G. F., Bindeman, I. N., Sobolev, A. V., Kuzmin, D. V., Ivanov, A. V., Woodhead, J. & Schilling, J. -G. (2017). Multiple mantle sources of continental magmatism: insights from "high-Ti" picrites of Karoo and other large igneous provinces. *Chemical Geology* **455**, 22–31. 10.1016/j.chemgeo.2016.08.034.

Klausen, M. B. (2009). The Lebombo monocline and associated feeder dyke swarm: diagnostic of a successful and highly volcanic rifted margin? *Tectonophysics* **468**, 42–62. 10.1016/j.tecto.2008.10.012.

Klemme, S. & O'Neill, H. S. C. (2000). The near-solidus transition from garnet lherzolite to spinel lherzolite. *Contributions to Mineralogy and Petrology* **138**, 237–248. 10.1007/s004100050560.

Klimm, K., Blundy, J. D. & Green, T. H. (2008). Trace element partitioning and accessory phase saturation during H_2O-saturated melting of basalt with implications for subduction zone chemical fluxes. *Journal of Petrology* **49**, 523–553. 10.1093/petrology/egn001.

Krein, S. B., Behn, M. D. & Grove, T. L. (2020). Origins of major element, trace element, and isotope garnet signatures in mid-ocean ridge basalts. *Journal of Geophysical Research: Solid Earth* **125**, e2020JB019612.

Lawver, L. A., Gahagan, L. M. & Dalziel, I. W. D. (1998). A tight fit-early Mezozoic Gondawna, a plate reconstruction perspective. *Memoirs of the National Institution of Polar Research, Special Issue* **53**, 214–229.

Lightfoot, P. C., Hawkesworth, C. J., Hergt, J., Naldrett, A. J., Gorbachev, N. S., Fedorenko, V. A. & Doherty, W. (1993). Remobilisation of the continental lithosphere by a mantle plume: major-, trace-element, and Sr-, Nd-, and Pb-isotope evidence from picritic and tholeiitic lavas of the Noril'sk District, Siberian Trap, Russia. *Contributions to Mineralogy and Petrology* **114**, 171–188. 10.1007/BF00307754.

Luttinen, A. V. (2018). Bilateral geochemical asymmetry in the Karoo large igneous province. *Scientific Reports* **8**, 5223. 10.1038/s41598-018-23661-3.

Luttinen, A. V. (2021). Dronning Maud Land Jurassic volcanism: volcanology and petrology. In: Smellie, J. L., Panter, K. S. & Geyer, A. (eds.) *Volcanism in Antarctica: 200 Million Years of Subduction, Rifting and Continental Break-up*. Geological Society Memoirs 55. The Geological Society, Bath, United Kingdom, 157–181. 10.1144/M55-2018-89.

Luttinen, A. V. & Furnes, H. (2000). Flood basalts of Vestfjella: Jurassic magmatism across an Archaean-Proterozoic lithospheric boundary in Dronning Maud Land, Antarctica. *Journal of Petrology* **41**, 1271–1305. 10.1093/petrology/41.8.1271.

Luttinen, A. V., Rämö, O. T. & Huhma, H. (1998). Neodymium and strontium isotopic and trace element composition of a Meso-zoic CFB suite from Dronning Maud Land, Antarctica: implications for lithosphere and asthenosphere contributions to Karoo magmatism. *Geochimica et Cosmochimica Acta* **62**, 2701–2714. 10.1016/S0016-7037(98)00184-7.

Luttinen, A. V., Zhang, X. & Foland, K. A. (2002). 159 Ma Kjakebeinet lamproites (Dronning Maud Land, Antarctica) and their implications for Gondwana breakup processes. *Geological Magazine* **139**, 525–539. 10.1017/S001675680200674X.

Luttinen, A. V., Leat, P. T. & Furnes, H. (2010). Björnnutane and Sembberget basalt lavas and the geochemical provinciality of Karoo magmatism in western Dronning Maud Land, Antarctica. *Journal of Volcanology and Geothermal Research* **198**, 1–18. 10.1016/j.jvolgeores.2010.07.011.

Luttinen, A. V., Heinonen, J. S., Kurhila, M., Jourdan, F., Mänttäri, I., Vuori, S. K. & Huhma, H. (2015). Depleted mantle-sourced CFB magmatism in the Jurassic Africa–Antarctica rift: petrology and $^{40}Ar/^{39}Ar$ and U/Pb chronology of the Vestfjella Dyke Swarm, Dronning Maud Land, Antarctica. *Journal of Petrology* **56**, 919–952. 10.1093/petrology/egv022.

Luttinen, A., Kurhila, M., Puttonen, R., Whitehouse, M. & Andersen, T. (2022). Periodicity of Karoo rift zone magmatism inferred from zircon ages of silicic rocks: implications for the origin and environmental impact of the large igneous province. *Gondwana Research* **107**, 107–122. 10.1016/j.gr.2022.03.005.

Mallik, A. & Dasgupta, R. (2012). Reaction between MORB-eclogite derived melts and fertile peridotite and generation of ocean island basalts. *Earth and Planetary Science Letters* **329-330**, 97–108. 10.1016/j.epsl.2012.02.007.

Manninen, T., Eerola, T., Mäkitie, H., Vuori, S., Luttinen, A., Sénvano, A. & Manhiça, V. (2008). The Karoo volcanic rocks and related intrusions in Southern and Central Mozambique. In: Pekkala, Y., Lehto, T. & Mäkitie H. (eds.) *GTK Consortium Geological Surveys in Mozambique 2002–2007*. Geological Survey of Finland Special Paper 48. Geological Survey of Finland, Espoo, Finland, 211–250.

Marsh, J. S., Hooper, P. R., Rehacek, J., Duncan, R. A. & Duncan, A. R. (1997). Stratigraphy and age of Karoo basalts of Lesotho and implications for correlations within the Karoo Igneous Province. In: Mahoney, J. J. & Coffin, M. F. (eds.) *Large Igneous Provinces: Continental, Oceanic, and Planetary Flooc Volcanism*. American Geophysical Union Geophysical Monograph **100**, 247–272, 10.1029/GM100p0247.

Marzoli, A., Bertrand, H., Youbi, N., Callegaro, S., Merle, R., Reisberg, L., Chiaradia, M., Brownlee, S. I., Jourdan, F., Zanetti, A., Davies, J. H. F. L., Cuppone, T., Mahmoudi, A., Medina, F., Renne, P. R., Bellieni, G., Crivellari, S., El Hachimi, H., Bensalah, M. K., Meyzen, C. M. & Tegner, C. (2019). The Central Atlantic Magmatic Province (CAMP) in Morocco. *Journal of Petrology* **60**, 945–996. 10.1093/petrology/egz021.

McDonough, W. F. & Sun, S. S. (1995). The composition of the Earth. *Chemical Geology* **120**, 223–253. 10.1016/0009-2541(94)00140-4.

Melluso, L., Beccaluva, L., Brotzu, P., Gregnanin, A., Gupta, A. K., Morbidelli, L. & Traversa, G. (1995). Constraints on the mantle sources of the Deccan Traps from the petrology and geochemistry of the basalts of Gujarat State (Western India). *Journal of Petrology* **36**, 1393–1432. 10.1093/petrology/36.5.1393.

Melluso, L., Mahoney, J. J. & Dallai, L. (2006). Mantle sources and crustal input as recorded in high-Mg Deccan Traps basalts of Gujarat (India). *Lithos* **89**, 259–274. 10.1016/j.lithos.2005.12.007.

Moulin, M., Fluteau, F., Courtillot, V., Marsh, J., Delpech, G., Quidelleur, X. & Gérard, M. (2017). Eruptive history of the Karoo lava flows and their impact on early Jurassic environmental

change. *Journal of Geophysical Research: Solid Earth* **122**, 738–772. 10.1002/2016JB013354.

Natali, C., Beccaluva, L., Bianchini, G. & Siena, F. (2017). Comparison among Ethiopia-Yemen, Deccan, and Karoo continental flood basalts of central Gondwana: Insights on lithosphere versus asthenosphere contributions in compositionally zoned magmatic provinces. In: Bianchini, G., Bodinier, J.-L., Braga, R. & Wilson, M. (eds.) *The Crust-Mantle and Lithosphere-Asthenosphere Boundaries: Insights from Xenoliths, Orogenic Deep Sections, and Geophysical Studies*. Geological Society of America Special Paper 526. Geological Society of America, Boulder, Colorado, USA, 191–215.

Neumann, E.-R., Svensen, H., Galerne, C. Y. & Planke, S. (2011). Multistage evolution of dolerites in the Karoo Large Igneous Province, Central South Africa. *Journal of Petrology* **52**, 959–984. 10.1093/petrology/egr011.

Palme, H. & O'Neill, H. S. C. (2014). Cosmochemical estimates of mantle composition. In: Holland, H. D. & Turekian K. K. (eds.) *Treatise on Geochemistry, Volume 2: Mantle and Core*. Oxford: Elsevier, 1–39, 10.1016/B978-0-08-095975-7.00201-1.

Rehácek, J. (1995) Chemical and paleomagnetic stratigraphy of basalts in Northern Lesotho, Karoo Province. Unpublished Ph.D. thesis, Washington State University.

Riley, T. R., Leat, P. T., Curtis, M. L., Millar, I. L., Duncan, R. A. & Fazel, A. (2005). Early-middle Jurassic dolerite dykes from Western Dronning Maud Land (Antarctica): identifying mantle sources in the Karoo large igneous province. *Journal of Petrology* **46**, 1489–1524. 10.1093/petrology/egi023.

Riley, T. R., Curtis, M. L., Leat, P. T., Watkeys, M. K., Duncan, R. A., Millar, I. L. & Owens, W. H. (2006). Overlap of Karoo and Ferrar magma types in KwaZulu-Natal, South Africa. *Journal of Petrology* **47**, 541–566. 10.1093/petrology/egi085.

Robinson, J. A. C. & Wood, B. J. (1998). The depth of the spinel to garnet transition at the peridotite solidus. *Earth and Planetary Science Letters* **164**, 277–284. 10.1016/S0012-821X(98)00213-1.

Rollinson, H. & Pease, V. (2021). *Using Geochemical Data to Understand Geological Processes*, 2nd edn. Cambridge: Cambridge University Press, 10.1017/9781108777834.

Rudnick, R. L. & Gao, S. (2003). Composition of the continental crust. In: Rudnick, R.L. (ed.) *Treatise on Geochemistry, Volume 3: The Crust*. Oxford: Elsevier, 1–64, 10.1016/B0-08-043751-6/03016-4.

Sell, B., Ovtcharova, M., Guex, J., Bartolini, A., Jourdan, F., Spangenberg, J. E., Vicente, J.-C. & Schaltegger, U. (2014). Evaluating the temporal link between the Karoo LIP and climatic–biologic events of the Toarcian Stage with high-precision U-Pb geochronology. *Earth and Planetary Science Letters* **408**, 48–56. 10.1016/j.epsl.2014.10.008.

Shellnutt, J. G. (2014). The Emeishan large igneous province: a synthesis. *Geoscience Frontiers* **5**, 369–394. 10.1016/j.gsf.2013.07.003.

Shellnutt, J. G. & Jahn, B.-M. (2011). Origin of late Permian Emeishan basaltic rocks from the Panxi region (SW China): implications for the Ti-classification and spatial–compositional distribution of the Emeishan flood basalts. *Journal of Volcanology and Geothermal Research* **199**, 85–95. 10.1016/j.jvolgeores.2010.10.009.

Shellnutt, J. G. & Pham, T. T. (2018). Mantle potential temperature estimates and primary melt compositions of the low-Ti Emeishan flood basalt. *Frontiers in Earth Science* **6**, 67. 10.3389/feart.2018.00067.

Shellnutt, J. G., Bhat, G. M., Wang, K.-L., Brookfield, M. E., Jahn, B.-M. & Dostal, J. (2014). Petrogenesis of the flood basalts from the early Permian Panjal Traps, Kashmir, India: geochemical evidence for shallow melting of the mantle. *Lithos* **204**, 159–171. 10.1016/j.lithos.2014.01.008.

Sobolev, A. V., Hofmann, A. W., Kuzmin, D. V., Yaxley, G. M., Arndt, N. T., Chung, S. -L., Danyushevsky, L. V., Elliott, T., Frey, F. A., Garcia, M. O., Gurenko, A. A., Kamenetsky, V. S., Kerr, A. C., Krivolutskaya, N. A., Matvienkov, V. V., Nikogosian, I. K., Rocholl, A., Sigurdsson, I. A., Sushchevskaya, N. M. & Teklay, M. (2007). The amount of recycled crust in sources of mantle-derived melts. *Science* **316**, 412–417. 10.1126/science.1138113.

Sun, S. S. & McDonough, W. F. (1989). Chemical and isotopic systematics of oceanic basalts: Implications for mantle composition and processes. In: Saunders, A. D. & Norry, M. J. (eds.) *Magmatism in the Ocean Basins*. Geological Society Special Publication 42. The Geological Society, Blackwell Scientific Publications, Oxford, United Kingdom, 313–345, 10.1144/GSL.SP.1989.042.01.19.

Svensen, H., Corfu, F., Polteau, S., Hammer, Ø. & Planke, S. (2012). Rapid magma emplacement in the Karoo large igneous province. *Earth and Planetary Science Letters* **325-326**, 1–9. 10.1016/j.epsl.2012.01.015.

Sweeney, R. J., Duncan, A. R. & Erlank, A. J. (1994). Geochemistry and petrogenesis of central Lebombo basalts of the Karoo igneous province. *Journal of Petrology* **35**, 95–125. 10.1093/petrology/35.1.95.

Tegner, C., Lesher, C. E., Larsen, L. M. & Watt, W. S. (1998). Evidence from the rare-earth-element record of mantle melting for cooling of the Tertiary Iceland plume. *Nature* **395**, 591–594. 10.1038/26956.

Turunen, S. T., Luttinen, A. V., Heinonen, J. S. & Jamal, D. L. (2019). Luenha picrites, Central Mozambique—messengers from a mantle plume source of Karoo continental flood basalts? *Lithos* **346-347**, 105152, 1–16. 10.1016/j.lithos.2019.105152.

Workman, R. K. & Hart, S. R. (2005). Major and trace element composition of the depleted MORB mantle (DMM). *Earth and Planetary Science Letters* **231**, 53–72. 10.1016/j.epsl.2004.12.005.

Xu, Y., Chung, S.-L., Jahn, B. & Wu, G. (2001). Petrologic and geochemical constraints on the petrogenesis of Permian–Triassic Emeishan flood basalts in southwestern China. *Lithos* **58**, 145–168. 10.1016/S0024-4937(01)00055-X.

Zhang, X., Luttinen, A. V., Elliot, D. H., Larsson, K. & Foland, K. A. (2003). Early stages of Gondwana breakup: the ^{40}Ar/^{39}Ar geochronology of Jurassic basaltic rocks from Western Dronning Maud Land Antarctica and implications for the timing of magmatic and hydrothermal events. *Journal of Geophysical Research: Solid Earth* **108**, B2449.

Zhang, L., Ren, Z.-Y., Handler, M. R., Wu, Y.-D., Zhang, L., Qian, S.-P., Xia, X.-P., Yang, Q. & Xu, Y.-G. (2019). The origins of high-Ti and low-Ti magmas in large igneous provinces, insights from melt inclusion trace elements and Sr-Pb isotopes in the Emeishan large igneous province. *Lithos* **344-345**, 122–133. 10.1016/j.lithos.2019.06.014.